

A spectroscopic survey of infrared 1-4 μ m spectra in regions of prominent solar coronal emission lines of Fe XIII, Si X, and Si IX

AATIYA ALI,^{1,2} ALIN RAZVAN PARASCHIV,^{1,3} KEVIN REARDON,¹ AND PHILIP JUDGE³

¹National Solar Observatory, 3665 Discovery Drive, Boulder, CO 80303, USA

²Georgia State University, 25 Park Place, NE #605, Atlanta, GA 30303, USA

³High Altitude Observatory, National Center for Atmospheric Research, Boulder CO 80307-3000, USA

(Received December 15, 2021; Accepted March 15, 2022)

Submitted to ApJ

ABSTRACT

The infrared solar spectrum contains a wealth of physical data about the Sun and is being explored using modern detectors and technology with new ground-based solar telescopes. One such instrument will be the ground-based Cryogenic Near-IR Spectro-Polarimeter of the Daniel K. Inouye Solar Telescope that will be capable of sensitive imaging of the faint infrared solar coronal spectra with full Stokes I, Q, U, and V polarization states. Highly ionized magnetic dipole emission lines have been observed in galaxies and the solar corona. Quantifying the accuracy of spectral inversion procedures requires a precise spectroscopic calibration of observations. A careful interpretation of the spectra around prominent magnetic dipole lines is essential for deriving physical parameters, and particularly, for quantifying the off-limb solar coronal observations from DKIST. In this work, we aim to provide an analysis of the spectral regions around the infrared coronal emission lines of Fe XIII 1074.68 nm, Fe XIII 1079.79 nm, Si X 1430.10 nm, and Si IX 3934.34 nm, aligning with the goal of identifying solar photospheric and telluric lines that will help facilitate production of reliable inversions and data products from four sets of solar coronal observations. The outputs will be integrated in the processing pipeline to produce Level-2 science-ready data that will be made available to DKIST observers.

Keywords: Solar corona (1483), Solar coronal lines (2038), Spectroscopy (1558), Galaxy spectroscopy (2171), Astronomy data analysis (1858)

1. INTRODUCTION

Two of the first-light instruments of the Daniel K Inouye Solar Telescope (DKIST, [Rimmele et al. 2020](#)) will perform spectropolarimetry of coronal lines in the infrared (IR) region: the Diffraction Limited Near IR Spectro-polarimeter (DL-NIRSP, [Elmore et al. 2014](#)) and the Cryogenic Near-IR Spectro-Polarimeter (Cryo-NIRSP, [Fehlmann et al. 2017](#)). This work focuses on surveying select spectral intervals around prominent coronal lines of Fe XIII, Si X, and Si IX, in the infrared 1-4 μ m range with the goal of identifying spectral features that can either influence interpretation of coronal measurements from the ground, or be used as references for science calibration. Figure 1 shows the four spectral windows of interest relevant to Cryo-NIRSP filters observing the above-mentioned coronal emission lines. We use the Coronal Line Emission (CLE) code (see [Casini & Judge 1999](#), for method description) to synthesize theoretical coronal emission of these lines. We aim to identify the effects of scattering and variable telluric absorption features to help obtain accurate physical measurements through the disentanglement of the coronal emission. The results of this analysis are required for developing science-ready “Level-2” coronal observations and data products.

Energetic emitting regions in astronomical sources have traditionally been studied via X-ray, ultraviolet (UV), optical, and infrared emission lines of highly ionized intermediate-mass elements. One of the first correct interpretations of forbidden lines was provided by [Edlén \(1943\)](#). Such lines are often referred to as “coronal lines” since the ions, when produced by collisional

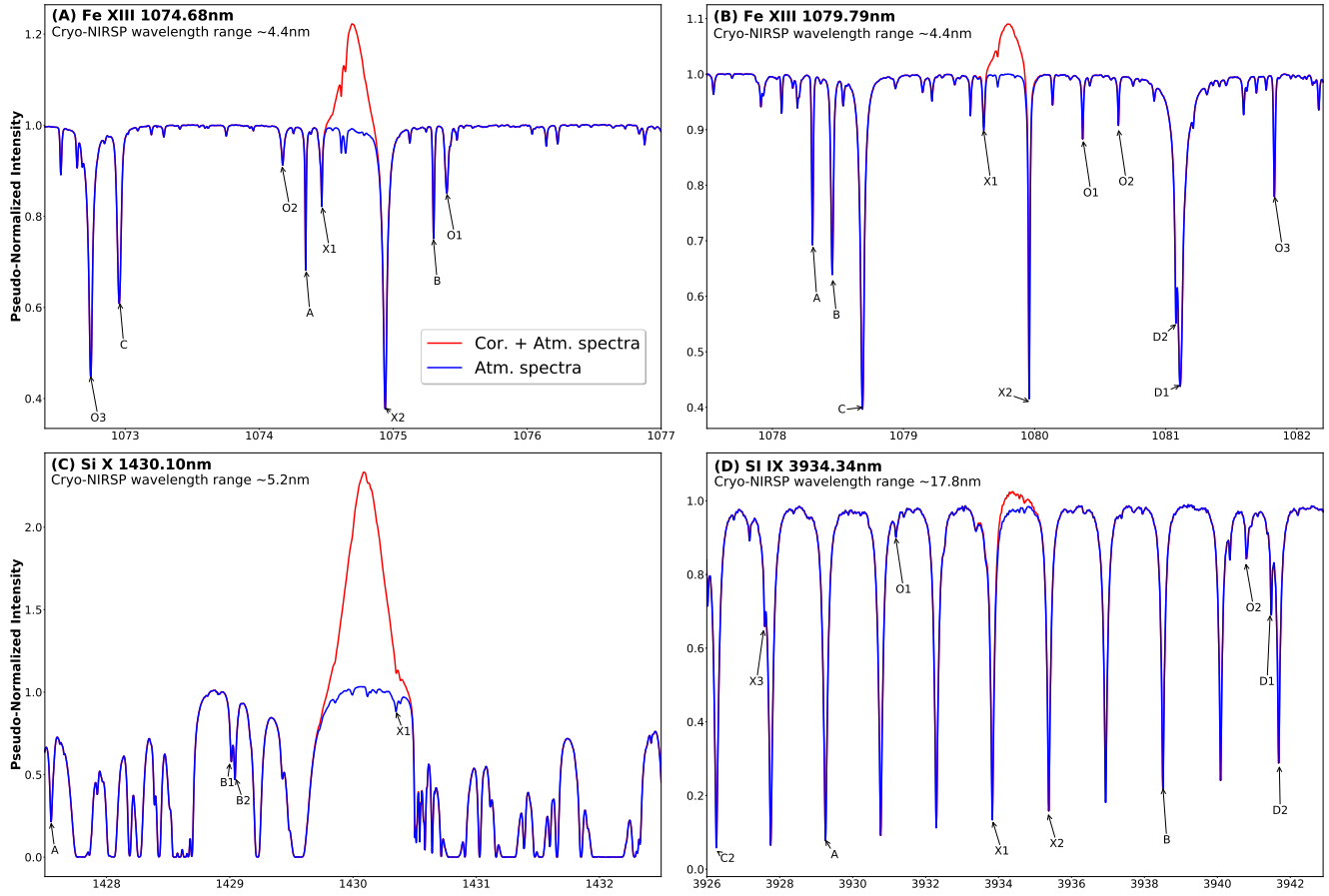


Figure 1. Coronal Line Emission (CLE) synthesized Fe XIII , Si X, and Si IX emission profiles are plotted over normalized atmospheric absorption spectra. Each coronal ion is centered over a usable wavelength range corresponding to a relevant Cryo-NIRSP filter. The theoretical coronal line intensities are scaled corresponding to estimations presented in Table 1 and then added over an atlas of atmospheric absorption spectrum. The absorption line labels are described in Table 3.

ionization, reach maximum abundance at electron temperatures of $\sim 10^5 - 10^6$ K (or 8.6 eV - 86 eV as measured by Feldman & Doschek (1977)), typical of the Sun's upper atmosphere (Greenhouse et al. 1993).

The emergence of sensitive infrared array detectors prompted existing atomic data to be reexamined for coronal lines sensitive at expected field strengths of orders around 10 G (Kuhn 1995). Polarized light from magnetic dipole (M1) lines contain information on coronal magnetic fields in two areas: the direction of the magnetic field projected onto the plane of the sky encoded in the observed linear polarization (Charvin 1965), and the strength and sign of the magnetic fields along the line of sight (LOS) encoded in the circular polarization (Harvey 1969; Judge et al. 2001; Lin et al. 2004). Casini & Judge (1999) present a compact formulation for the description of polarized radiation from M1 transitions occurring in the magnetized solar corona, accounting for the influence of the scattered radiation on atomic polarization induced through both anisotropic irradiation and the Zeeman effect. Plowman (2014), Dima & Schad (2020), Judge et al. (2021), and Paraschiv & Judge (2022) incrementally build upon each other to develop practical methods for inverting magnetic field information from polarized coronal observations.

The most promising lines lie between 1 and 10 μm , with the lower limit set by the need to detect small field strengths; and the upper limit by small Einstein A-coefficients and lower intensities of photospheric light (Judge 1998), with particular emphasis given to astrophysically abundant ions formed in the solar corona (those with partly filled shells principal quantum numbers $n = 2, 3$) with M1 transitions spanning a broad range of wavelengths (Schiffmann et al. 2021). The most promising lines include Fe XIII at 1074.68 nm and 1079.79 nm, as well as Si X at 1430.10 nm, as recorded during the 1998 eclipse and discussed in Judge (1998). Kuhn et al. (1999) further studied the emission line of Si IX at 3934.34 nm, and found consistent results. We chose these IR coronal emission M1 lines as targets for our work.

These lines have been under analysis and speculation for over two decades now for their atomic properties. For example, Si IX has forbidden transitions that hold promise to be diagnostics of coronal magnetic fields (Brage et al. 2000). Of the M1 lines

further studied by [Judge et al. \(2006\)](#), those of Fe XIII and Si X are particularly promising because of their relatively strong polarization. All four spectral lines will be observed using Cryo-NIRSP¹ where they are part of the main spectral diagnostics to be targeted, as introduced by [Fehlmann et al. \(2016\)](#).

The feasibility of coronal observations of Si X and Si IX was first established theoretically by [Münch \(1966\)](#). The radiated power in the lines was predicted by the authors, and found to be large enough to make their detection plausible. Relative to the sky, the brightest predicted emission line observed in the nucleus of a Seyfert galaxy is from the Si IX emission line at 3934.34 nm ([Oliva et al. 2001](#)). Its detection in the solar corona was one of the primary goals the airborne IR filter-based imaging observations of [Kuhn et al. \(1999\)](#), although the authors were unable to independently confirm the central wavelength of the 3934.34 nm filters to better than a few nanometers. [Penn et al. \(1994\)](#) hypothesized that the strong Si IX emission line may be the brightest IR coronal emission line to ever be detected.

[Judge et al. \(2002\)](#) reported a rest wavelength for the line and suggested its potential use as a diagnostic of coronal magnetic fields using the ground-based McMath-Pierce telescope based at the Kitt Peak Observatory ([Pierce 1964](#)). These observations gave the $\lambda_{rest} = 3.93434 \pm 0.00007 \mu m$ where the blue wing of the Si IX emission line overlaps a strong telluric N_2O line (see Figure 3 of [Judge et al. \(2002\)](#)). This observation is matched by us when interpreting the Si IX calibration candidate lines analyzed in Table 3, and portrayed in Figures 1 and 12. By “candidates” we mean absorption lines which we identify herein that can be used to calibrate velocity shifts and, if needed, to retrieve the un-attenuated coronal spectrum. Further, these observations show the Si IX 3934.34 nm line being present in active regions of the sun, with intensity levels higher than expected. This may be due to variations in the silicon abundance in the corona, allowing it to remain a strong choice for coronal magnetometry ([Judge et al. 2002](#)).

Exhibiting linear polarization of magnitude and direction agreeing with resonance polarization theory, measurements produced with the Fe XIII 1074.68 nm line by [Eddy & McKim Malville \(1967\)](#) indicated that the degrees of polarization were somewhat below what was anticipated in a corona with strict radial magnetic fields, a result confirmed by [Arnaud & Newkirk \(1987\)](#). Deviations of the field by 20° to 30° from the radius vector were consistent with measured degrees of polarization. We now know that the degrees of polarization signals can be alternatively explained by fields that might not be in the plane of sky, but cross the integrated volume of a voxel ([Paraschiv & Judge 2022](#)). The estimated abundances relative to hydrogen produced in the [Eddy & McKim Malville \(1967\)](#) analysis (see their fig. 5) agree with iron abundances in the corona.

Later, [Penn & Kuhn \(1994\)](#) found comparable brightness in the Fe XIII lines. This is also consistent with [Penn et al. \(1994\)](#), who found Si X and Fe XIII emissions to again be of comparable brightness, although the derived Si X intensity is higher than ground-based measurements.

Successive detections of Si X and of Fe XIII were performed by [Kuhn et al. \(1996\)](#), via an airborne experiment during the 1994 eclipse, and ground-based observations obtained by the non-coronagraphic McMath-Pierce solar telescope were also used in this experiment. Sensitive measurements of the near-IR coronal spectrum obtained during this eclipse confirmed again through statistical processes that the Si X emission line at 1430.10 nm has a brightness comparable to the 1074.68 nm Fe XIII emission line. It was hypothesized to be sensitive to magnetic fields 40% smaller when compared with Fe XIII and was consequently proposed as a good choice for coronal magnetometry ([Kuhn et al. 1996](#)).

More recently, [Judge et al. \(2019\)](#) surveyed spectra at thermal IR wavelengths and presented broadband polarized light data captured during the 2017 total solar eclipse while testing new technologies for measuring polarized coronal light. Spectra of the limb photosphere, chromosphere, prominences, and coronal lines from 310 nm to 5.5 μm were all analyzed for this experiment. These observations were taken by an airborne IR coronal imaging spectrometer flown above Kentucky, and a new IR Fourier Transform Spectrometer (FTS) was also deployed from Wyoming. The new FTS offered a particularly high resolution spectra, allowing for the assessment of detailed telluric absorption profiles for new emission lines measured from the aircraft. The aforementioned Si IX line was one of the lines again under analysis. The authors found that the architecture and modernity of the instruments were still inadequate to detect coronal lines from low-altitude sites due to various sensitivities such as atmospheric absorption and background. The Airborne Infrared Spectrometer (AIR-Spec) was constructed with the goal of studying several magnetically sensitive coronal lines, assessing their validity to pursue as future spectro-polarimetric observations ([Samra et al. 2018](#)). The combination of the moderate-resolution FTS and AIR-Spec spectra therefore clearly revealed for the first time the effects of telluric extinction on the IR coronal emission lines.

The coronal IR spectrum over the range of wavelengths observable by DKIST remains sparsely sampled, and the eclipse of 2017 offered the opportunity to explore this wavelength range in advance of DKIST operations. Motivations secondary to assessing detailed telluric absorptions include searching IR regions for magnetically sensitive coronal lines. Ultimately, AIR-Spec sampled

¹ Cryo-NIRSP instrument summary document

very little of the IR spectra. It is possible that unexpected lines exist in the infrared corona that have not yet been detected. This is why exploring the information in these spectral regions, is a worthwhile goal that will help in the further understanding of the sun's corona.

Emission-line measurements may reveal the presence and nature of current systems in the corona (Judge et al. 2006), motivating the need to develop instruments capable of measuring polarized light in forbidden coronal lines, such as the DKIST's Cryo-NIRSP. Whether additional ions, e.g. Mg VIII \sim 3028nm, are detectable in ground observations is still debatable. Theoretical intensity calculations and older observational runs are reserved (Münch 1966; Olsen et al. 1971; Judge 1998), but a definitive ruling has not been reached, as discussed by Judge et al. (2001) and Samra et al. (2018). For this reason, we limited our coronal line selection to encompass only the more reliable Fe XIII, Si X, and Si IX ions.

This work is therefore critical to prepare for meaningful observations of coronal M1 lines on a routine basis. The necessity mentioned by Judge (1998) for improved measurements to assess the completeness and accuracy of theoretical spectroscopic work is important to note, aligning with conclusions of needing to perform high resolution spectral analysis of absorption spectra in proximity of coronal emission, shown by Judge et al. (2019). This kind of analysis can be performed on data like the airborne AIR-Spec measurements analyzed by Samra et al. (2018), or data obtained from ground-based instruments like the FTS provided via the high-resolution McMath-Pierce atlas, which we utilize here. The aforementioned experiments performed, as well as the data products and properties derived from them, all reaffirm the practicality to inspect the neighboring regions of our four chosen coronal lines.

The organization of this work is as follows: the architecture and limitations of the instruments and observations used are described in Section 2. The analysis procedure and obtained outputs are presented in Section 3, followed by the results along with potential issues that can arise in Section 4. Finally, our conclusions are presented in Section 5. The detailed spectroscopic analysis and best fits for each of the different candidates of Fe XIII, Si X, and Si IX absorption lines are included in Appendix A.

2. OBSERVATIONS, INSTRUMENTATION, & MODELING

DKIST is an off-axis capable telescope. Its Cryo-NIRSP instrument is designed as coronagraph. It was designed to take full advantage of this capability by primarily observing the 1-5 μ m range, a region of low scattered light with enhanced sensitivity to the Zeeman effect. The telescope configuration provides the ability to conduct unobstructed off-axis observations. Cryo-NIRSP is mounted on the DKIST Coudé platform and will measure the full polarization state (Stokes I, Q, U, and V) solar spectral lines at wavelengths ranging between \sim 1000 nm - 5000 nm, using one of two slits: one of length 233'' and width 0''.5 with a spectral resolving power of \sim 30000; and the second slit of length 120'' and width of 0''.15 with a spectral resolving power of \sim 100000. Effective pixel platescales and resolutions will be dependent on the combination of slit and filter in use (see Nelson et al. 2010; Fehlmann et al. 2016). For this work, we considered the most updated instrumental parameters in [1] and quote resolutions of 0.027 nm, 0.027 nm, 0.033 nm, and 0.107 nm (lower spectral res. 0''.5 slit) along with 0.008 nm, 0.008 nm, 0.011 nm, and 0.036 nm (higher spectral res. 0''.15 slit) corresponding to the Fe XIII, Si X, and Si IX wavelength ranges, respectively.

To harness the multitude of advantages of operating at IR wavelengths, Cryo-NIRSP must be cryogenically cooled to \sim 70 K to reduce any background noise that could compromise the faint solar coronal signal (Fehlmann et al. 2017). Cryo-NIRSP is the DKIST instrument with the dedicated capability of sensitively imaging the relatively faint IR corona and thermal IR solar spectrum. Its polarimetric and spectrographic capabilities will allow measurements of the faint coronal emission with unprecedented cadence, resolution, and accuracy.

In the current facility configuration, Cryo-NIRSP can not work in conjunction with other DKIST instruments and does not utilize the DKIST Wavefront Correction (WFC) system. Thus, increased uncertainties arising due to mixing of different spatial positions may manifest, especially in the case of longer integration times and the narrower 0''.15 slit.

We also briefly mention the DKIST DL-NIRSP diffraction grating based integral field spectrograph, that has a low resolution mode of 0''.93 in the 500 nm – 1800 nm wavelength range (Elmore et al. 2014). Our analysis is also relevant for DL-NIRSP as our selected lines of Fe XIII and Si X might be simultaneously observable by two of the three bands (900 nm – 1350 nm and 1350 – 1800 nm) with full Stokes polarization.

Our four selected coronal line emission profiles are synthesized using CLE and scaled based on theoretical or observed literature intensities. The available literature has debated over which conditions coronal line intensities can be measured from ground instrumentation, airborne instrumentation or via balloon flights (e.g. Penn & Kuhn 1994; Kuhn et al. 1999; Lin et al. 2004; Penn 2014; Samra et al. 2018; Judge et al. 2019; Samra et al. 2021). Theoretical calculations for coronal line intensities at heights of \sim 1.1 R_{\odot} were computed by Judge (1998), and adapted by us in Table 1. Theoretical intensities for infrared lines including those of coronal ions have been reviewed more recently by Del Zanna & DeLuca (2018) where the authors stress that the atomic data requires improvements. We note for these strongest lines the conclusions of Judge (1998) currently remain valid.

Table 1. A compilation of relative to background coronal line intensities derived from literature observations. Ground, eclipse, flight and balloon campaigns are considered. Due to the limited number of intensity calibrated observations available in the literature, we show only relative to background values. Theoretical intensity calculations at $\sim 1.1 R_{\odot}$ are adapted from Judge (1998, Fig. 3) and are in units of $\text{erg cm}^{-2} \text{s}^{-1} \text{st}^{-1}$.

Cor. line	Theoretical Int.	Observed Rel. Int.	Exp. Time	Source
		1.2	40	Fig. 3
Fe XIII 1074.68nm	22.4	1.4	5	Bao et al. (2009)
		1.5	40-70	Singh et al. (2002)
		4.6	120	Penn (2014)
		1.2	40	Fig. 3
Fe XIII 1079.79nm	5.2	1.1	5	Bao et al. (2009)
		1.1	40-70	Singh et al. (2002)
		2.4	120	Penn (2014)
Si X 1430.10nm	5.4	2.3	5	Dima et al. (2018)
		4.4	120	Penn (2014)
Si IX 3934.34nm	0.7	1.0	300	Penn (2014)

At this time, Cryo-NIRSP is still being integrated into the DKIST facility, and there is no available data that can be used for the purposes of this work. Our spectral line identifications will be performed using an “atlas” of high spectral resolution calibrated observations compiled from the FTS instrument of the McMath-Pierce telescope (Wallace et al. 1996; Dulick et al. 2001). The FTS is able to obtain ground-based spectral data by reconstructing the interference pattern of vacuum frequency observations. The FTS is capable of obtaining spectra from approximately $22 \mu\text{m}$ to $0.7 \mu\text{m}$, with resolving power and resolution limited by the total path difference obtainable with the spectrometer. The FTS atlas spectra covers all of our four regions of interest with resolutions of 0.0004 nm, 0.0004 nm, 0.0013 nm, and 0.0080 nm respectively for each coronal ion wavelength range.

In order to validate and test our FTS atlas identifications, we utilized observed coronal spectra encompassing the two Fe XIII lines in the 1074 nm - 1080 nm IR regions, as analyzed by (Singh et al. 2002) using observations done at the Norikura Observatory. The coronal spectral observations were performed with a 25cm aperture refracting coronagraph. A CCD camera mounted on the system, has a pixel size of $24 \mu\text{m} \times 24 \mu\text{m}$ with a 1024 x 1024 format allowing for the observation of a 6 nm portion of the spectrum. The achieved spectral resolution was ~ 0.018 nm, which is comparable with the Cryo-NIRSP values listed above. The pixel resolution of the spectroheliograms after binning the CCD readout was approximately $2'' \times 2''$ but the slit width that was equivalent to $4''$ on the Sun, which restricted the spatial sampling to about $2'' \times 4''$ (Singh et al. 2002).

3. METHODOLOGY

Understanding the origins and magnitude of the contamination of ground-based observations would overall aid in the interpretation of observed coronal data and prepare it for data analysis and assist in the automation of the processing of the data acquired by DKIST. When discussing polarised observations, we focus here on interpreting the Stokes I component, as Stokes Q, U, and V are formally just derivatives of I (Casini & Judge 1999). The goal for DKIST coronal Level-2 data processing is to invert physical coronal information from raw Level-1 Stokes profiles obtained using Cryo-NIRSP coronal line observations. Addressing neighboring photospheric absorption and telluric absorption lines will further reduce uncertainties introduced through the observations, and provide guidance on how to reduce and reliably calibrate observations of these same lines in more broad galactic applications and possibly in future stellar coronae observations.

3.1. Searching for Photospheric & Atmospheric Lines Suitable for Interpreting Coronal Emission

We start by searching for photospheric and telluric absorption profiles in proximity to the 1074.68 nm, 1079.79 nm, 1430.30 nm, and 3934.34 nm wavelength ranges using the FTS Kitt Peak spectral atlas. The FTS atlas was corrected for wavelength conversions from the vacuum to air values in all three spectral windows of interest using the approximation provided by Ciddor (1996). By proximity, we mean we selected windows, of the size of the spectral range covered by the Cryo-NIRSP prefilters, in which each of the four Fe XIII, Si X, and Si IX lines, were centered in the respective interval. The widths of the spectral intervals are 4.4 nm for the Fe XIII 1074.68nm and 1079.79nm lines, 5.2 nm for Si X 1430.10 nm, and 17.8 nm for Si IX 3934.34 nm.

We then assessed which absorption lines to treat as candidates by utilizing the BAsE de données Solaires Sol² (BASS2000) high resolution solar spectrum database (Abouadarham & Renié 2020). Each potential absorption line was searched for in the database to ensure that it was not a spurious effect portrayed as a phantom dip in the spectra. In addition, we did not consider "weak" lines, defined herein as having a drop of less than 0.1 in relative intensity (column 7 in Table 3) in the FTS atlas. The lines can saturate in their cores, making identification of their centroid difficult, were also not considered. The absorption features were then verified using the BASS2000 database and were subsequently deemed usable in the case of positive identification, or deemed unusable by not finding a corresponding profile in BASS2000. This procedure also served as a double check for the confidence of the FTS atlas.

The National Institute of Standards and Technology (NIST) Atomic Spectra Database³ (ASD; Kramida et al. 2020) was then used to assess the air wavelengths for the chosen photospheric absorption lines from the spectra, and to subsequently identify them. The identifications usually matched the centroid wavelengths of the FTS atlas. In some cases, minimal differences on the order of < 0.01 nm between the ASD and the FTS atlas were found. These differences might become significant in the context of achievable wavelength calibrations. Further, the ASD contains information on the relative line intensity and the transition probability A_{ki} that was utilized to confirm that the respective transition is indeed the one responsible for our observed absorption profile.

So far, the focus has been on photospheric absorption profiles. We now shift our attention to potential molecular telluric candidate absorptions. Ground-based observations using the non-coronagraphic McMath-Pierce telescope (Judge et al. 2002) have provided observed spectra of telluric molecular absorption lines in the IR regions. Therefore, when identifying molecular absorptions that would not be otherwise covered by the NIST ASD database, we utilized Penn (2014, Figure 1) (originally presented in Hinkle et al. 2003) that catalogs atmospheric transmission in the IR 0.5 - 5.5 μm range, to single out plausible molecules. We then utilized the high-resolution transmission (HITRAN) molecular absorption database⁴ (Gordon et al. 2017) to confirm our identification as follows: The observed air wavelengths, confirmed using BASS2000, that could not be associated with any NIST ASD atomic lines were converted to vacuum wavenumbers, and then queried with the HITRAN output of the singled-out molecules in each desired wavelength range. All HITRAN findings are obtained with main isotopologue molecular sequences, with an abundance > 0.99 . The HITRAN line intensity S and Einstein Coefficient A (analogous to ASD's A_{ki}) are utilized to confirm the identification of each suitable line. The HITRAN wavenumbers are then converted back to air wavelengths. Similar differences on the order of < 0.01 nm between HITRAN data and the FTS atlas are reported in a limited number of cases. HITRAN wavelength calculations and intensities are presented in Table 3 for identified lines of H₂O (Tennyson et al. 2013; Mikhailenko et al. 2016; Toth 1995a; Tennyson et al. 2013), N₂O (Toth 1995b), CH₄ (Daumont et al. 2013; Hilico et al. 2001), and SO₂ (Naumenko & Horneman 2019) molecules.

Shown in Figure 1 are the Fe XIII, Si X, and Si IX selected spectral ranges in which various candidate absorption lines were identified and analyzed using statistical processes discussed in Section 4. The pseudo-normalized units here reflect the FTS atlas being normalized to a local continuum value of unity, and the coronal synthesized spectra intensities being scaled relative to this continuum and added to the background counts. The relative to background coronal intensities shown are calculated using estimations collated in Table 1, that are then added to background spectra. Currently, we have very few measurements of the relative line emission with respect to the background. This is further complicated by the variation in the background intensity, which depends on the amount of scattered light from the sky and telescope optics. An example of an actual Si IX observation that is the "weakest" line in our set, is presented in Judge et al. (2002, Fig. 3). Our estimation of the Si IX intensity in panels D of Figures 1 and 5 also provide an example of how intensity might manifest in practical observations.

The line identifications are recorded in Table 3. The identification procedures are described in Section 3.3. The properties of all the absorption candidate lines are shown for each spectral window corresponding to one coronal line, as labeled in the

² BASS2000 survey spectra

³ NIST atomic spectral data query form

⁴ HITRAN molecular spectra query form

first column. The second column records the identifying labels for each analyzed absorption profile. The labelling of the lines identified in Table 3 follow three categories: alphabetical (e.g. A, B, C, D1, D2, etc.), “O” lines (e.g. O1, O2, etc.), and “X” lines (e.g. X1, X2, etc.), with respect to each of the four selected wavelength ranges. The alphabetical category consists of lines identified using the FTS atlas and confirmed with BASS2000 and the NIST ASD database or identified using HITRAN. The second category are lines considered as back-up candidates that might be used in certain conditions, while the last category of lines were those that were found problematic to interpret. Such problems may involve: saturated intensity counts; very weak absorption profiles; overlap with the coronal emission lines centered in the spectral window assuming no Doppler shifts are occurring; or when lines become uncertain when convolving the FTS atlas with Cryo-NIRSP instrumental specifications, etc. The implications of Table 3 are expanded in Section 4.3.

The comments might describe lines that do not have a clear corresponding atomic or molecular emission at those wavelengths, or in some cases, lines that are portrayed by ASD or HITRAN to correlate to a transition that should not be strong enough, or to an atom that does not have a minimal solar abundance (i.e. Th I accidentally corresponding to 1074.17 nm, etc.). Given these discrepancies in identification of some of these lines, not all are considered by us suitable for disentangling the coronal emission. Appendix Figures 6, 8, 10, and 12 show the detailed spectral positions and characteristics of all the absorption line identifications presented in Table 3, that are corresponding to the spectral windows associated to each of our four coronal lines of interest.

3.2. Spectral Line Fitting

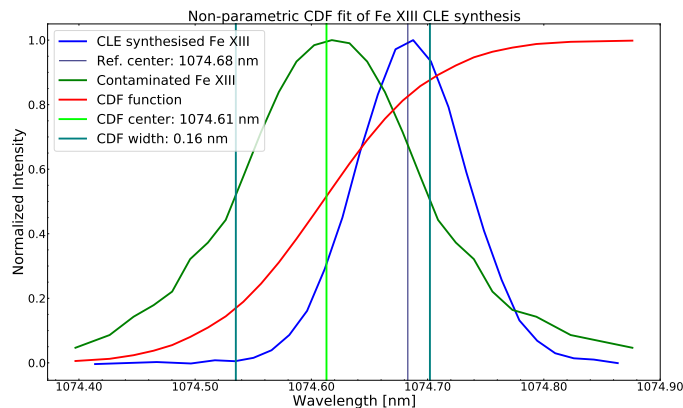


Figure 2. CDF non-parametric fitting applied to synthetic CLE Stokes I coronal spectra for the Fe XIII 1074.68 nm line. The blue emission profile represents the synthesized theoretical atomic emission, while the green profile depicts the same profile after it has been contaminated by wavelength shifts and profile broadening due to atmospheric air column movements and turbulence. The Red curve represents the CDF fit of the contaminated Fe XIII line.

We employ a non-parametric method, using the Cumulative Distribution Function (CDF) to pre-process the coronal Stokes I profiles and lines identified in the FTS atlas. This simple, yet robust statistical method allows general line properties to be quantified using intensity measurements (see example in Figure 2). The method is more general than standard Gaussian fitting as it enables us to sum data as a function of wavelength, and interpret it in a statistical fashion. The fitting method is used herein on both coronal emission and absorption lines from spectral data. In practice, we take the main line parameters resulted from the CDF fit and used them as initial parameters for a curve fitting algorithm, in order to obtain sub-pixel accuracy. A meaningful interpretation requires the assumption that the Stokes I profiles are compatible with a normal distribution. The achievable spectral resolution of the Cryo-NIRSP spectrograph will also cause most profiles to be similar to normal distributions. Under the limitations of our data and for the goals of this work, we therefore consider this assumption to be satisfied.

Statistical methods applied to the CDFs of Stokes intensity vs. wavelength can be used to derive the properties of the lines, where the wavelengths corresponding to the 16%, 50%, and 84% of the normalized distribution are recovered. For a true normal distribution, this 16-84% range corresponds to $\sim 2\sigma$, where σ correlate to the standard deviation of a normal distribution.

Parameters that can be recovered using this approach include wavelength shifts, and from it, Doppler velocities, as well as line widths, and uncertainties. In particular, wavelength shifts can then be calculated from the difference between the distribution centroid wavelength (50%) and a laboratory value. In Figure 2, Stokes I profiles of Fe XIII coronal emission in ideal (pure) and noise influenced conditions (contaminated by turbulence which would mix different spatial locations in the same pixel, lowering the spatial resolution and mixing multiple profiles) are synthesized by us using CLE. Table 2 presents a comparison between

Table 2. Example of non-parametric CDF and parametric Gaussian fitting for CLE a synthesized Fe XIII 1074.68 nm observation. The pure synthesized observation is compared to an uncertainty contaminated version of itself. The CDF analysis is applied to the contaminated spectra. The Gaussian width here is 2σ , and the CDF width is defined as the difference between 84th and 16th percentiles.

	Contaminated Fe XIII	Pure Fe XIII
CDF 50th (Median)	1074.61	1074.68
CDF 84th	1074.69	1074.74
CDF 16th	1074.54	1074.63
CDF Width [nm]	0.16	0.11
Gauss Mean	1074.61	1074.68
Gauss Width [nm]	0.14	0.11

CDF and Gaussian fitting, where both perform almost identically in the idealized case. The non-parametric approach is seen to be more flexible in more complex cases.

In general, our method aims to isolate coronal emission lines in observed spectra, extract their main parameters via CDF analysis, then use these to perform a detailed curve fit to finely tune these extracted parameters. We then search for usable absorption profiles in the same wavelength range, perform the same type of fitting on these, and then look for differences when comparing them with a laboratory/database reference positions, enabling us to use such differences to calibrate the coronal line. In order to extract the parameters using this CDF based approach for our absorptions of interest identified in Section 3.1, we selected small spectral windows so that the line under scrutiny was isolated without any other absorption influences. Some lines were very hard to isolate; e.g. the spectral range around the 1430.10 nm Si X emission as shown in Figure 10. Some combinations of two adjacent lines are also selected and documented in Table 3. These are fitted with a custom CDF approach suited for multi-peak identification.

3.3. Validating the Spectral Identification and Fitting

Raw observational spectra from the Norikura Observatory were used in conjunction with the identifications corresponding to the two Fe XIII lines to observationally validate the survey identifications, and show that these absorption lines can be used in ground observations to calibrate coronal emission. The identified photospheric and atmospheric absorptions in Table 3 are compared to the raw spectral observations. In practice, these raw Norikura observations were checked against the FTS atlas, where observed central wavelengths and depth of absorptions were then compared to the identified lines. A visual comparison between raw Norikura spectra and the corresponding FTS atlas subrange is shown in Figure 3. Figure 4 presents problems that might appear when trying to utilize these atlas candidates with actual observations. This is expanded in Section 4.2.

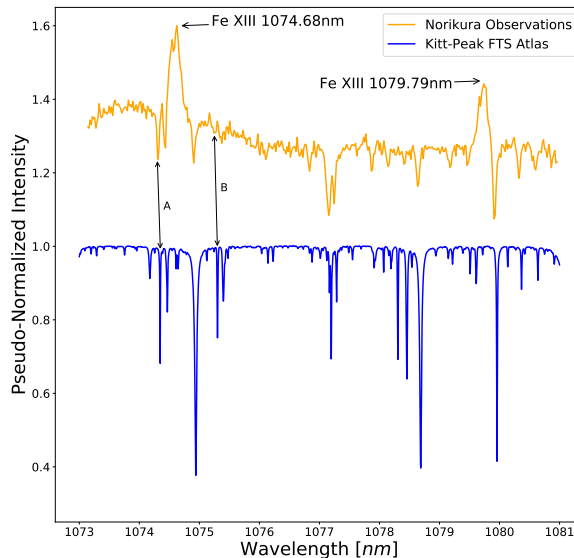


Figure 3. Norikura Observations compared to the Kitt Peak FTS atlas in the Fe XIII spectral window against a pseudo-normalized intensity. These spectra were compared in order to determine the best choices for the candidate lines for analysis for the Fe XIII coronal line. Here, the Norikura Observations are slightly shifted vertically to clearly visualize both spectra. The labels A and B identify two absorption lines for the Fe XIII 1074.68 nm coronal line, as observed by the Norikura Observatory. The individual line fits are expanded in Figure 4.

4. RESULTS AND DISCUSSION

4.1. Coronal Line Intensities

Figure 5 depicts examples of expected observation for the four coronal lines under scrutiny, showing estimated coronal intensities and how typical coronal LOS outflow velocities influence their spectroscopic observations. Additionally, we did not normalize the integration time to counts per second for the relative intensities in Table 1 due to not being able to distinguish in all sources whether the line cores are saturated due to instrumental or physical effects. The theoretical intensities adapted in Table 1, although being inconclusive by themselves, raise compelling questions that can be pursued via DKIST Cryo-NIRSP observations.

The observed relative intensities, adapted via Table 1, corroborate with the findings of Samra et al. (2018) resulting from eclipse observations taken above the atmosphere. Additional weaker coronal ions like Mg VIII at 3027.64 nm were detected from those altitudes. We bring to attention Figure 5 (D) showing that “expected” intensities for the Si IX line are weak with respect to the background and close to detection limits, based on the current available observations and theoretical intensity estimations. This leads us to consider Si IX as representing a detection baseline for this selection. We did not further provide estimations for other scientifically interesting coronal lines like the Mg VIII line mentioned above that are the target of Cryo-NIRSP due to the uncertainty of high-confidence detection from the ground, even for an instrument like Cryo-NIRSP. Thus, we consider our four discussed coronal lines to represent the best candidate choices for coronal spectro-polarimetry and magnetic field diagnostics, as they are strong enough to be observed from the ground with next generation instrumentation like Cryo-NIRSP.

Due to the yet inconclusive nature of current observations, we chose to present the Appendix Figures 6, 8, 10, and 12 as an overlap of CLE synthesized coronal emission and the FTS atlas spectra, using just pseudo-normalized units where coronal emission is scaled arbitrarily between 1 and 2, without considering the above discussed intensity calculations.

We reaffirm the need for improvements needed in atomic and theoretical intensity calculations, as correlating different coronal observations proved difficult due to difference in instrumentation, observation conditions, locations, height matching, integration times, and scarce absolute intensity calibrations.

4.2. Comparing Atmospheric Absorption Spectra with Coronal Observations

Figure 3 plots both the FTS atlas spectra and Norikura spectra analyzed by Singh et al. (2002) for one spectral position at $\sim 1.1 R_{\odot}$, in the range covering both Fe XIII coronal lines. In Figure 4 (left), we portray the results of the analysis applied to one

example absorption line in the Fe XIII spectral window. The selected line, centered at ~ 1074.35 nm could not be identified in the ASD database. Instead, a HITRAN H₂O candidate line was confirmed. The FTS atlas is plotted with the raw observation over the same spectral range. Both of these had the CDF analysis applied to them. The center positions of the distributions are marked and were calculated from the distribution statistics as described in Section 3.2. The spectral sampling of the raw observation is significantly coarser than that of the FTS atlas. Taking this into account, we show that the CDF method does recover the centroid of the absorption, with an uncertainty mainly given by the spectral sampling of 0.0187 nm. We draw attention to the spectral positions between the two spectra, highlighting a 0.041 nm shift that is present in the raw observation. This shift likely indicates an error in the definition of the absolute wavelength scale of the Norikura data, which depends on orbital motions, solar rotation, and instrumental alignment and drifts. This is important in context as modern instruments will achieve resolutions of orders of magnitude more significant; e.g. Cryo-NIRSP will reach pixel resolutions in the order of 0.009 nm. In addition, we take note that in this case, a small difference exists between the FTS atlas CDF line center and the theoretical ASD or HITRAN air wavelength. This small 0.004 nm difference, correspondent to a ~ 1 km s⁻¹ Doppler velocity, might be due to the uncertainty of the spectral sampling of the FTS atlas, or by a not-as-accurate identification of the ASD air wavelength. Either way, this difference is negligible towards our effort, as it is smaller than what even a next generation instrument like Cryo-NIRSP can resolve as measuring such a difference in the highly broadened coronal lines will be challenging.

All the candidate calibration lines for both Fe XIII coronal lines were scrutinized in the same way, revealing and confirming the same atmospheric shifts, as for the purpose of this example we only used one time instance in the raw observation. We could not obtain similar raw observations in the Si X and Si IX spectral windows, as these are significantly less studied.

In Figure 4 (right) we show a more convoluted example of an identification, also in the Fe XIII spectral window. As recorded in Table 3, the absorption line B at 1075.30 nm is a candidate selected for analysis, identified as a photospheric Fe I absorption line in the ASD. We applied the CDF methods to both the FTS atlas and observed spectra as in the above example, and found that in this instance the observed spectra's CDF peak was at ~ 0.055 nm to the right of the ASD and FTS atlas central wavelengths. This immediately indicated that there was a problem during the semi-automated analysis of the data, since this is the same instance of the observation as in Figure 4 (left), subjected to the same atmospheric conditions. Although higher resolution spectra from the FTS atlas and BASS2000 allowed for the identification of the line with a reasonable 0.75 absorption dip, the line was too weak in the raw observation to permit recovery. Thus, the procedure incorrectly fitted an unrelated line in the sampled spectral range. In order to avoid such problems, we set up our procedure to fit multiple absorption lines in conjunction, (e.g. A, B, and C) across the Fe XIII spectral window, comparing the independent determinations, and automatically rejecting outliers.

4.3. Sets of Potential Calibration Lines for Coronal Observations

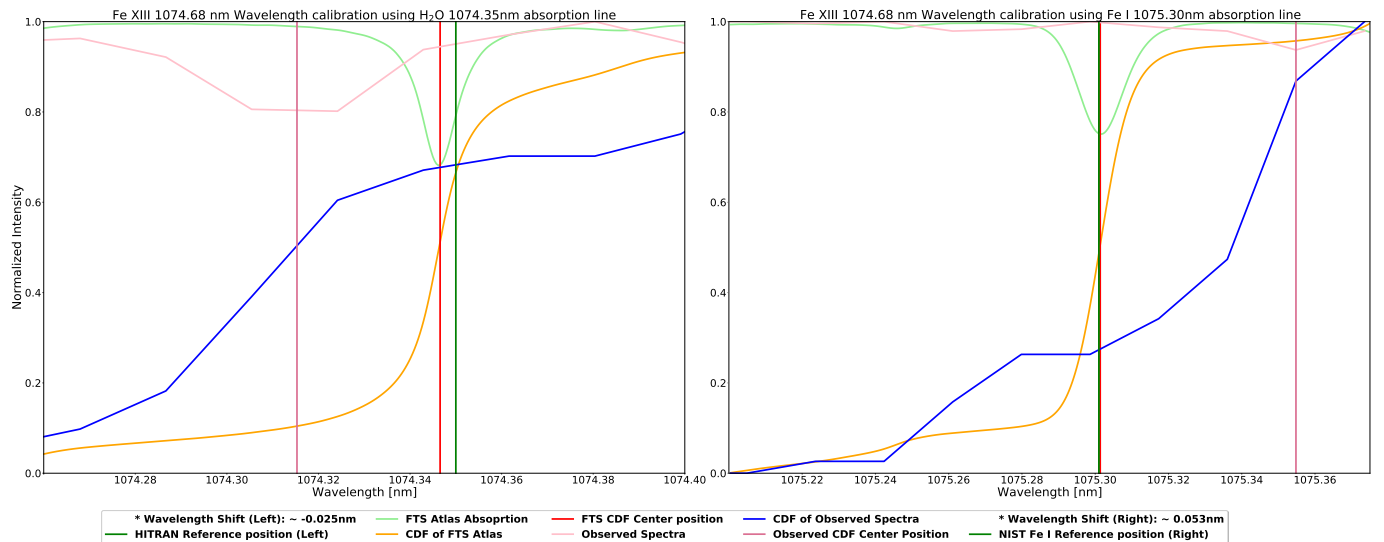


Figure 4. Identified calibration lines are used to calibrate the Fe XIII 1074.68 nm coronal line. The FTS atlas spectra is plotted with the raw observation, revealing atmospheric shifts that will influence or even compromise coronal observations. Left Panel: Fe XIII wavelength calibration using the H₂O 1074.35 nm absorption line. Right Panel: Incorrect wavelength calibration while using the "B" Fe I 1075.30 nm photospheric absorption line identified in Table 3. The line could not be isolated in the particular time instance of the raw observation, leading to a bad fit. The effect can be corrected by coupling multiple identified lines in the analysis.

Table 3. Candidate absorption lines for atmospheric shift calibration as respective to the four spectral windows corresponding to the chosen coronal lines. Not all candidate lines could be identified in the NIST ASD database. The Wavelength column follows the FTS atlas, HITRAN or ASD air wavelength when they match. In the case of small differences between the two or when a HITRAN or ASD identification could not be made, the FTS atlas wavelength is quoted. Some absorption lines could not be separated, and should be analyzed as a pair. Numbered letters eg. O1,O2,... or X1, X2,... are less desirable due to weak or saturated absorption profiles, overlap the main coronal lines, etc.

Cor. Line & Wave.	ID	Cal. Line	Source	Wave.	CDF Wave. Range	Rel. I	Comment
Fe XIII 1074.68nm	O3	Si I	ASD	1072.74nm	1072.58nm - 1072.92nm	0.44	Very strong line; too close to slit wavelength margin
	C	C I	ASD	1072.95nm	1072.84nm - 1073.12nm	0.60	Strong absorption line
	O2	H ₂ O	HITRAN	1074.15nm	1073.96nm - 1074.32nm	0.91	Very weak line; Cryo-NIRSP detection uncertain
	A	H ₂ O	HITRAN	1074.35nm	1074.24nm - 1074.44nm	0.68	Strong absorption. Blend of two water lines
	X1	Fe I	ASD	1074.46nm	1074.40nm - 1074.52nm	0.82	Weak line, unusable due to blend with cor. Fe XIII line
	X2	Si I	ASD	1074.94nm	1074.80nm - 1075.10nm	0.38	Strong line, unusable due to blend with cor. Fe XIII line
	B	Fe I	ASD	1075.30nm	1075.20nm - 1075.37nm	0.75	Not very prominent but might be usable
	O1	C I	ASD	1075.40nm	1075.31nm - 1075.46nm	0.85	Weak line; possible blend issue
	A	Fe I	ASD	1078.30nm	1078.20nm - 1078.40nm	0.69	Strong absorption line
	B	Si I	ASD	1078.45nm	1078.32nm - 1078.58nm	0.63	Strong absorption line
Fe XIII 1079.79nm	C	Si I	ASD	1078.68nm	1078.48nm - 1078.96nm	0.39	Very strong line
	X1	H ₂ O	HITRAN	1079.60nm	1079.56nm - 1079.70nm	0.89	Weak line. Strong blend with cor. Fe XIII line
	-	-	-	-	-	-	Unusable due to blend with cor. Fe XIII line
	X2	H ₂ O	HITRAN	1079.95nm	1080.32nm - 1080.40nm	0.41	Strong line. Blend of two water lines
	-	-	-	-	-	-	Unusable due to blend with cor. Fe XIII line
	O1	H ₂ O	HITRAN	1080.37nm	1080.16nm - 1080.56nm	0.88	Weak line; Weak blend with cor. Fe XIII line; Cryo-NIRSP detection uncertain
	O2	Ne I	ASD	1080.63nm	1080.56nm - 1080.72nm	0.91	Very weak line; Cryo-NIRSP detection uncertain
	D2	H ₂ O	HITRAN	1081.08nm	1080.72nm - 1081.52nm	0.56	Strong absorption 2-line set. Weak for Cryo-NIRSP lower spectral res.
	D1	Mg I	ASD	1081.11nm	1080.72nm - 1081.52nm	0.43	Strong absorption 2-line set; treat as pair
	O3	Fe I	ASD	1081.83nm	1081.64nm - 1082.04nm	0.77	Moderately strong line; close to slit wavelength margin
Si X 1430.10nm	A	Fe I	ASD	1427.50nm	1427.48nm - 1427.62nm	0.21	Separable line in tough range; needs specialized fitting procedure
	B1	H ₂ O	HITRAN	1429.01nm	1428.83nm - 1429.14nm	0.47	Pair of close lines, fit together; Weak for Cryo-NIRSP lower spectral res.
	B2	H ₂ O	HITRAN	1429.04nm	1428.83nm - 1429.14nm	0.57	Blend with B1
	X1	Fe I	ASD	1430.30nm	1430.29nm - 1430.34nm	-	Not usable due to blend with cor. Si X line; Cryo-NIRSP detection uncertain
	C1	CH ₄	HITRAN	3926.02nm	3925.48nm - 3927.08nm	0.71	Weak for Cryo-NIRSP lower spectral res. couple with N ₂ O band
	C2	N ₂ O	HITRAN	3926.26nm	3925.48nm - 3927.08nm	0.06	Molecular absorption to couple with C1
	X3	CH ₄	HITRAN	3928.68nm	3928.62nm - 3928.72nm	0.67	Not usable due to proximity to N ₂ O molecular band
	A	N ₂ O	HITRAN	3929.25nm	3928.12nm - 3930.28nm	0.08	Molecular absorption band
	O1	N ₂ O	HITRAN	3931.17nm	3931.00nm - 3931.40nm	0.90	Weaker N ₂ O line; Cryo-NIRSP detection uncertain
	X1	N ₂ O	HITRAN	3933.83nm	3933.32nm - 3936.52nm	0.13	Absorption band; not usable due to blend with cor. Si IX line
Si IX 3934.34nm	X2	N ₂ O	HITRAN	3935.38nm	3933.32nm - 3936.52nm	0.15	Absorption band; not usable due to blend with cor. Si IX line
	B	N ₂ O	HITRAN	3938.50nm	3938.12nm - 3938.92nm	0.22	Molecular absorption band
	O2	SO ₂	HITRAN	3940.80nm	3940.44nm - 3941.24nm	0.84	Weak line. Weak S in HITRAN. Blend with weak water line
	D1	CH ₄	HITRAN	3941.47nm	3941.16nm - 3942.12nm	0.69	Blend of two methane lines. Couple with N ₂ O band
	D2	N ₂ O	HITRAN	3941.66nm	3941.16nm - 3942.12nm	0.29	N ₂ O Molecular band for D1

Every absorption candidate line’s spectral position and label, as recorded in Table 3, can be visualized in Figures 6, 8, 10, and 12. The high resolution spectra for each selected candidate line can be found in the four subsections of appendix A, corresponding to each of the four spectral windows in Figures 7, 9, 11, and 13. The CDF method is applied to the absorption spectra for each scrutinized line, and their centers are compared to their NIST ASD or HITRAN reference positions. Note that the absorption profiles of these panels are reversed into emission for the ease of reading each plot.

The alphabetical category of labeling in the ID column encompasses lines that have deep absorption profiles, with a minimum residual intensity of <0.8 . For most of them, we could identify the corresponding atom in the ASD or the HITRAN atmospheric molecular absorptions by using Penn (2014). In general cases, these lines can be isolated in the spectra, but more convoluted situations exist. In some cases, multiple lines affected by blending need to be analyzed as a pair; e.g. D1 and D2 in the spectral window of Fe XIII 1079.79 nm. Additionally, all lines in this category are not close to the edge of our chosen spectral windows.

The second category of lines encompasses those where one or more of the criteria described for the above category is not satisfied. For example, we use Figure 6 and scrutinize line O3, finding it to have very strong absorption, but is too close to the left end of the Cryo-NIRSP prefilter wavelength range to routinely use in the analysis process. In the same spectral window, lines O1 and O2 are both weak lines. The “O” lines can be weaker than 0.8 residual intensity, but we have not chosen candidates weaker than 0.91. As shown in Figure 4 (right), weaker lines might not be reliable by themselves in non-ideal conditions.

The third category of lines were those that were either very weak or overlapping the not-Doppler shifted coronal emission lines within the spectral range. These lines were identified, labeled, and quantified in order to understand and mitigate the effects of the underlying spectra on coronal emission, but were deemed weaker candidates due to uncertainties caused by this blending. In Figure 6, lines X1 and X2 overlap and blend with the Fe XIII coronal emission. We note that our synthesized Fe XIII emission encompasses only thermal effects that dictate the broadening. In an actual observation, the emission will probably be significantly broader, principally due to unresolved plasma motions along the LOS (Billings 1966). These lines become usable in situations where significant Doppler shifts are observed, as shown in Figure 5.

Figures 6, 8, 10, and 12 also present the effects of applying a convolution of the atmospheric spectra with a Gaussian function having a full width at half maximum (FWHM) of the Cryo-NIRSP nominal spectral resolution in the wavelength range for each selected coronal line. This showed that all the labels defined using the criteria above remain valid even for actual Cryo-NIRSP observations.

Column four then documents the sources that were utilized to identify each absorption line. The two sources are the ASD for atomic lines or HITRAN for molecular lines. The air wavelengths, as recovered from one of the sources, were cross-checked with the FTS atlas and BASS2000. The resulting wavelengths are then recorded in column five.

The calculated relative intensities are determined using the FTS atlas and represent the difference of the absorption peak from the normalized background of the spectra. Brief, specific notes per candidate line made are also recorded on the 7th column of Table 3.

4.4. Absorption Wavelength Range and Accuracy

Column six of Table 3 records usable ranges for CDF fitting for all discussed absorption profiles. Some closely spaced lines (as described in the comments) might benefit from a multi-peak fitting approach, which requires computing derivatives of the CDF profiles. Alternatively, the profiles can also be directly fitted with more standard parametric function approaches inside the same wavelength ranges and Double-Gaussian functions can be used where required. Based on the ASD and HITRAN identification and/or Penn (2014) analyses, we separated the identified line into photospheric absorption and terrestrial molecular absorptions. The interpretation for atmospheric based molecular absorptions like N₂O in the Si IX spectral window is straightforward. Atmospheric lines from molecules of N₂O, H₂O, CH₄, and SO₂ are considered to be very stable. The accuracy in using such lines for calibrations has been established by Caccin et al. (1985) to be in order of 0.05 km s^{-1} . The base estimation was more recently confirmed by Figueira et al. (2010), where additional corrections can improve the accuracy to up to 0.02 km s^{-1} . In our context, deviations from the rest wavelength are interpreted as being due to shifts in telluric columns and the profile broadening or narrowing caused by a change in local opacity. Solar photospheric lines like Fe I, Si I, C I, etc. require a different interpretation. These should exhibit roughly weak Doppler velocities, corresponding to photospheric movements on the order of $0.5\text{-}1 \text{ km s}^{-1}$ (e.g. Asplund & Collet 2003; Rempel 2011; Welsch et al. 2013) where transitory flows of the order of $\sim 5 \text{ km s}^{-1}$ might occur (Nagata et al. 2008). These movements will generally cancel-out as in such cases, the light in this background is derived from the atmospheric scattering of full-disk contributions of photospheric light. Orbital motions of the Earth might also influence these lines.

On the other hand, coronal outflows can have velocities in the order of tens to hundreds of km s^{-1} . For example, recent spectroscopy of coronal jets revealed outflow speeds in between $17\text{-}170 \text{ km s}^{-1}$ (Zhang et al. 2021). In the cases of large impulsive

ejecta, like Coronal Mass Ejection (CMEs) outflows can routinely reach velocities of over 1000 km s^{-1} in extreme examples (see Zhang et al. 2004; Bein et al. 2011, and references therein). Additionally, in open coronal regions, propagation of acoustic waves is $\sim 150 \text{ km s}^{-1}$, and typical Alfvénic wave propagation velocities are on the order of $400\text{-}600 \text{ km s}^{-1}$ (see Morton et al. 2015). Not all observational cases will encompass outflowing structures. There is significant interest in analyzing more subtle motions in the corona on the order of $1\text{-}5 \text{ km s}^{-1}$ (e.g. Tomczyk et al. 2007). For this exercise all velocities should be considered upper limits as we did not take into account projection effects.

Figure 5 shows how typical LOS outflow speeds can influence a spectral observation. For this, we overlapped the FTS atlas spectra with a CLE simulation of coronal emission with encoded LOS outflow speeds of $\pm 5, \pm 20, \pm 50, \pm 150, \text{ and } \pm 400 \text{ km s}^{-1}$. For three of the four panels, two versions of the plots are provided. The highest LOS speed is only plotted for panel (D) as it is the only region where the Cryo-NIRSP slit is wide enough to recover such speeds.

The top plots show the Doppler shifted coronal lines with the pseudo-normal intensity units described in Section 4.1. We observe how certain absorption lines might become detectable against the shifted or broader/narrower coronal emission line profiles. In other words, lines that are normally not recommended might be used as good calibration candidates in certain conditions, thus the inclusion in the list. Taking this effect into account, we advise that any calibration line selection method should dynamically select the most optimal calibration lines, based on the raw spectral position of the coronal line center.

The bottom plots show calculated intensities that simulate the observed relative intensity values provided in Table 1. The weakest intensities were selected as corresponding to each coronal line, as to provide a cautious overview of how strongly these lines manifest in a real observation. As can be seen especially in panel D, a very cautious and meticulous pre-processing is needed in order to recover the coronal emission with respect to the background, which is expected to vary considerably depending on local conditions at the observatory.

The wavelength ranges of the long Cryo-NIRSP slits for the Fe XIII and Si X ions will be insufficient to analyze very fast moving coronal LOS velocities or Alfvénic waves as described above, when centering the slits on the rest wavelengths of the ions in question. As dynamically changing diffraction grating angle with the Cryo-NIRSP is not currently provisioned, Si IX is a recommended choice for such studies due to the significantly larger slit spectral coverage. We can observe in panel D, that in this case, interpretation is hindered by the low predicted and observed coronal signal, but also due to the very deep and closely spaced N_2O band absorption lines.

We finally remind the reader that when dealing with single vantage point observations, e.g. Cryo-NIRSP observations, any observed velocity might be only a small fraction of a true velocity due to projection effects. If we thus assume a required velocity accuracy in coronal measurements to be on the order of $\sim 1 \text{ km s}^{-1}$, this will lead to a wavelength calibration accuracy of $\sim 0.004 \text{ nm}$ at 1074.68 nm , and $\sim 0.013 \text{ nm}$ at 3934.34 nm . The future commencement of DKIST observations will put this requirement to the test.

5. SUMMARY AND FUTURE PROSPECTS

This work focused on surveying certain narrow windows in the infrared spectra around $1\text{-}4 \mu\text{m}$ to identify suitable spectroscopic lines that detrimentally and systematically change the coronal data, but which can be used to calibrate highly ionized coronal magnetic dipole lines emitted by solar but also by galaxies. The extreme dimness of stellar coronae compared with photospheres make such lines undetectable in the absence of high quality coronagraphs occulting regions very close to the photosphere, something not yet achieved in exo-planetary imaging. The resolution and quality of the observed spectra used in this paper is in some cases below the quality of data that will be attained by modern large aperture instruments like Cryo-NIRSP, nevertheless our analysis and results of absorption spectra offer a baseline list of wavelengths calibrations that can help to interpret coronal emission observed by facilities such as the novel DKIST.

To summarize:

- Modern instruments like Cryo-NIRSP will observe IR solar coronal data with a sensitivity never obtained before. The instrument can not use adaptive optics corrections, making it prone to contamination effects that need correcting before quantitatively analyzing observations.
- To this purpose, this work focuses on analyzing spectral windows in the IR in proximity to the outstanding solar coronal lines of Fe XIII 1074.68 nm , Fe XIII 1079.79 nm , Si X 1430.10 nm , and Si IX 3934.34 nm .
- We identify and analyze absorption profiles using the NIST ASD or HITRAN databases in the relevant spectral windows corresponding to our four chosen coronal emission lines, and confirm the results by cross-checking the BASS2000 survey spectra.
- We identify lines of both solar (photospheric) and atmospheric absorption (molecular line), and quantify their properties. Additionally, we discuss that in the context of expected coronal LOS Doppler shifts, the identified lines can be used to provide accurate values of coronal Doppler shifts.

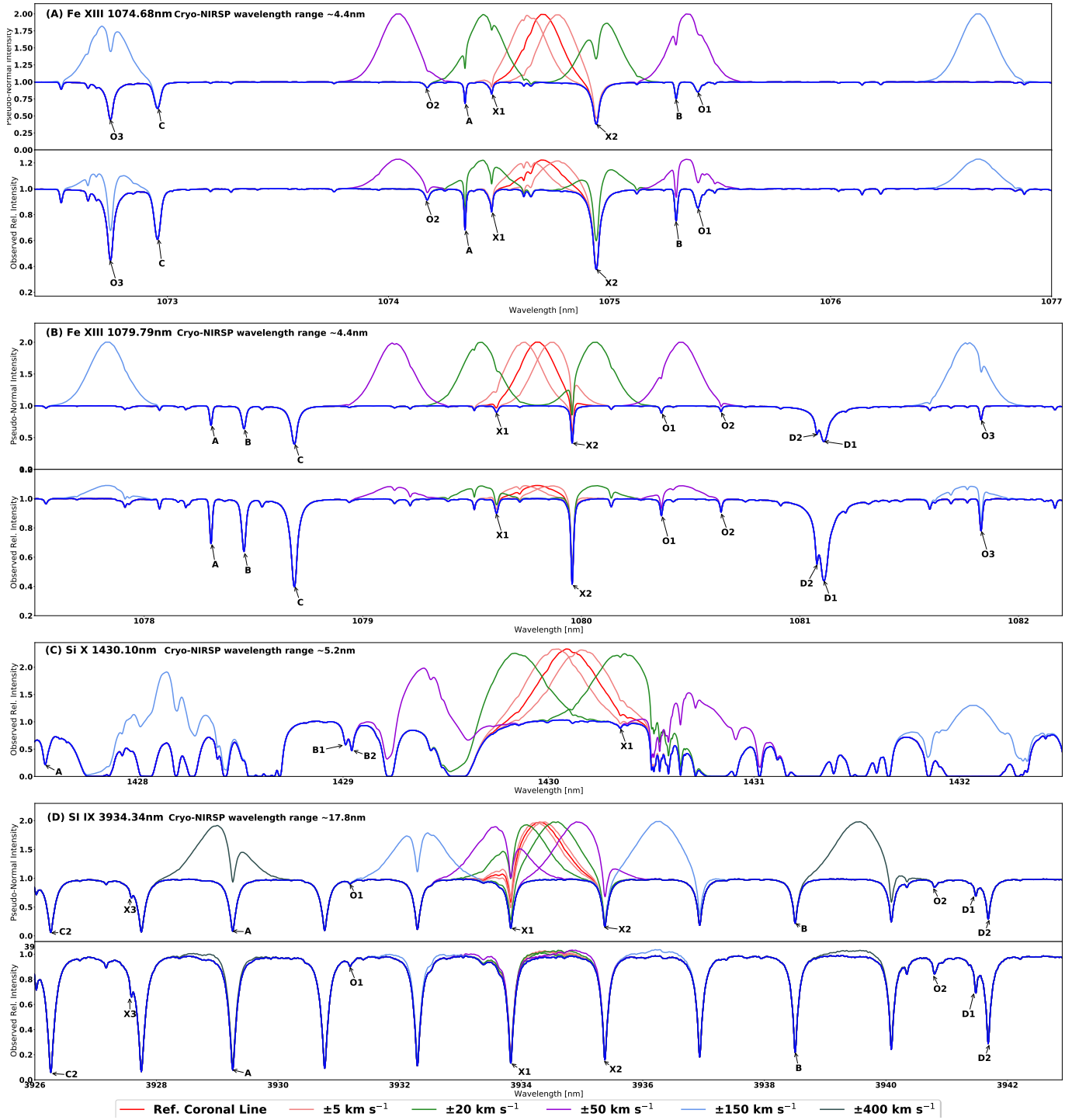


Figure 5. Multiple blue-red Doppler shifts of ± 5 , ± 20 , ± 50 , ± 150 , and ± 400 (panel D only) km s^{-1} are applied to the simulated coronal emission and then combined with the FTS atlas spectra, over wavelength ranges equivalent to the relevant Cryo-NIRSP prefilters. For panels A, B, and D, plots using both pseudo-normal counts (top) and observationally derived relative intensities (bottom) and are provided. The weakest intensities from Table 1 are chosen. In the case of panel C, only the observed relative intensity is plotted because counts are similar in both interpretations. In the case of panel D, The wavelength is sufficiently large to analyze high-speed streaming coronal plasma, although, as can be seen, the background relative intensity will complicate interpretation.

- Our categorizing of the candidates from their absorption spectra provides new information that can be utilized to adequately quantify the spectral properties of coronal IR emission lines of interest. We note that absolute and relative intensities remain an open question and can not be constrained with the methods described here.
- The validation for the absorption profiles in the Fe XIII spectral range via the comparison with raw observations provided a basic understanding of the varying observational conditions that could influence the future observations DKIST will perform.
- Although our CDF based fitting method proved reliable, our testing of the calibration procedure showed that in poor observing conditions, some profiles might not be accurately recovered, leading to errors in the analysis. We mitigate this by simultaneously using the combination of all clearly identifiable absorption candidate lines when performing a coronal calibration.
- The relative intensity calculations derived from previous observations show that some of the coronal lines in question might be hard to disentangle from background signal.
- Strong absorption profiles and in the case of Si X low transmission manifest in the spectral windows of interest. The influence of such identified absorption lines on coronal emission is not negligible. This is further complicated when dealing with outflowing plasma. DKIST observations might, in some cases, require advanced planning, including additional calibration data, when expecting highly Doppler shifted spectra.
- Quantifying the level of contamination that could affect observations and enhance the recovery of spectral properties and results from coronal observations is a goal not covered in this work. Our future aim is to use these spectroscopic results to assess the quality of a potential coronal observation.

The results presented in Table 3 are of particular importance when preparing data for addressing and inverting coronal magnetic field information - a goal of DKIST's Cryo-NIRSP and DL-NIRSP instruments. The same issues will need to be addressed for accurately resolving magnetic fields in future larger field-of-view (FOV) instrumentation, like COSMO (Thompson et al. 2018) and UCoMP (Tomczyk & Landi 2019), both of which will provide novel observations that can augment DKIST data.

ACKNOWLEDGMENTS

The authors thank the anonymous reviewer for her/his comments that greatly helped us improve this work. We additionally thank D.A. Lăcătuș for the careful reading and review of the initial submission. BASS2000 Data have been obtained thanks to the IR solar spectrum obtained from Kitt Peak observations. BASS2000 website has been used to get those data. Data from the NIST atomic spectra database queried via the NIST ASD website. The Norikura observation used by us as a validation dataset was provided via courtesy of T. Ichimoto.

A.A. was funded by the National Science Foundation (NSF) Boulder Solar Alliance REU program, award #1659878. A.R.P. and K.R. were funded by the National Solar Observatory (NSO), a facility of the NSF, operated by the Association of Universities for Research in Astronomy (AURA), Inc., under Cooperative Support Agreement number AST-1400405. P.J. was funded by The National Center for Atmospheric Research, sponsored by the National Science Foundation.

REFERENCES

- Abouadarham, J., & Renié, C. 2020, BASS2000, database of Solar ground-based observations, doi: [10.25935/9TXJ-F095](https://doi.org/10.25935/9TXJ-F095)
- Arnaud, J., & Newkirk, G., J. 1987, *A&A*, 178, 263
- Asplund, M., & Collet, R. 2003, in *Astronomical Society of the Pacific Conference Series*, Vol. 293, 3D Stellar Evolution, ed. S. Turcotte, S. C. Keller, & R. M. Cavallo, 197. <https://arxiv.org/abs/astro-ph/0302408>
- Bao, X., Zhang, Z., Deng, J., et al. 2009, *Science in China: Physics, Mechanics and Astronomy*, 52, 1794, doi: [10.1007/s11433-009-0235-6](https://doi.org/10.1007/s11433-009-0235-6)
- Bein, B. M., Berkebile-Stoiser, S., Veronig, A. M., et al. 2011, *ApJ*, 738, 191, doi: [10.1088/0004-637X/738/2/191](https://doi.org/10.1088/0004-637X/738/2/191)
- Billings, D. E. 1966, *A guide to the solar corona* (New York: Academic Press)
- Brage, T., Judge, P. G., Jönsson, P., & Edwards, D. P. 2000, *ApJ*, 540, 1114, doi: [10.1086/309383](https://doi.org/10.1086/309383)
- Caccin, B., Cavallini, F., Ceppatelli, G., Righini, A., & Sambuco, A. M. 1985, *A&A*, 149, 357
- Casini, R., & Judge, P. G. 1999, *ApJ*, 522, 524, doi: [10.1086/307629](https://doi.org/10.1086/307629)
- Charvin, P. 1965, *Annales d'Astrophysique*, 28, 877
- Ciddor, P. E. 1996, *ApOpt*, 35, 1566, doi: [10.1364/AO.35.001566](https://doi.org/10.1364/AO.35.001566)
- Daumont, L., Nikitin, A. V., Thomas, X., et al. 2013, *Journal of Quantitative Spectroscopy and Radiative Transfer*, 116, 101, doi: [10.1016/j.jqsrt.2012.08.025](https://doi.org/10.1016/j.jqsrt.2012.08.025)
- Del Zanna, G., & DeLuca, E. E. 2018, *ApJ*, 852, 52, doi: [10.3847/1538-4357/aa9edf](https://doi.org/10.3847/1538-4357/aa9edf)
- Dima, G. I., Kuhn, J. R., Mickey, D., & Downs, C. 2018, *ApJ*, 852, 23, doi: [10.3847/1538-4357/aa9e87](https://doi.org/10.3847/1538-4357/aa9e87)

- Dima, G. I., & Schad, T. A. 2020, *ApJ*, 889, 109, doi: [10.3847/1538-4357/ab616f](https://doi.org/10.3847/1538-4357/ab616f)
- Dulick, M., Plymate, C., & Wagner, J. 2001, One-Meter Fourier Transform Spectrometer
- Eddy, J. A., & McKim Malville, J. 1967, *ApJ*, 150, 289, doi: [10.1086/149330](https://doi.org/10.1086/149330)
- Edlén, B. 1943, *ZA*, 22, 30
- Elmore, D. F., Rimmele, T. R., Casini, R., et al. 2014, in , Vol. 9147 (Proc SPIE), 7, doi: [10.1117/12.2057038](https://doi.org/10.1117/12.2057038)
- Fehlmann, A., Giebink, C., Kuhn, J. R., Mickey, D. L., & Scholl, I. 2017, in AAS/Solar Physics Division Abstracts #48, AAS/Solar Physics Division Meeting, 117.02
- Fehlmann, A., Giebink, C., Kuhn, J. R., et al. 2016, Ground-based and Airborne Instrumentation for Astronomy VI, 9908, 99084D
- Feldman, U., & Doschek, G. A. 1977, *J. Opt. Soc. Am.*, 67, 726, doi: [10.1364/JOSA.67.000726](https://doi.org/10.1364/JOSA.67.000726)
- Figueira, P., Pepe, F., Lovis, C., & Mayor, M. 2010, *A&A*, 515, A106, doi: [10.1051/0004-6361/201014005](https://doi.org/10.1051/0004-6361/201014005)
- Gordon, I. E., Rothman, L. S., Hill, C., et al. 2017, *JQSRT*, 203, 3, doi: [10.1016/j.jqsrt.2017.06.038](https://doi.org/10.1016/j.jqsrt.2017.06.038)
- Greenhouse, M. A., Feldman, U., Smith, H. A., et al. 1993, *ApJS*, 88, 23, doi: [10.1086/191813](https://doi.org/10.1086/191813)
- Harvey, J. W. 1969, PhD thesis, National Solar Observatory
- Hilico, J.-C., Robert, O., Loëte, M., et al. 2001, *Journal of Molecular Spectroscopy*, 208, 1, doi: [10.1006/jmsp.2001.8364](https://doi.org/10.1006/jmsp.2001.8364)
- Hinkle, K. H., Wallace, L., & Livingston, W. 2003, in American Astronomical Society Meeting Abstracts, Vol. 203, 38.03
- Judge, P., Casini, R., & Parashiv, A. R. 2021, *ApJ*, 912, 18, doi: [10.3847/1538-4357/abebd8](https://doi.org/10.3847/1538-4357/abebd8)
- Judge, P., Berkey, B., Boll, A., et al. 2019, *SoPh*, 294, 166, doi: [10.1007/s11207-019-1550-3](https://doi.org/10.1007/s11207-019-1550-3)
- Judge, P. G. 1998, *ApJ*, 500, 1009, doi: [10.1086/305775](https://doi.org/10.1086/305775)
- Judge, P. G., Casini, R., Tomczyk, S., Edwards, D. P., & Francis, E. 2001, Coronal Magnetometry: A Feasibility Study, NASA STI/Recon Technical Report N
- Judge, P. G., Low, B. C., & Casini, R. 2006, *ApJ*, 651, 1229, doi: [10.1086/507982](https://doi.org/10.1086/507982)
- Judge, P. G., Tomczyk, S., Livingston, W. C., Keller, C. U., & Penn, M. J. 2002, *ApJL*, 576, L157, doi: [10.1086/343730](https://doi.org/10.1086/343730)
- Kramida, A., Yu. Ralchenko, Reader, J., & and NIST ASD Team. 2020, NIST Atomic Spectra Database (ver. 5.8), Available: <https://physics.nist.gov/asd> [2021, April 3]. National Institute of Standards and Technology, Gaithersburg, MD.
- Kuhn, J. R. 1995, in Infrared tools for solar astrophysics: What's next?, ed. J. R. Kuhn & M. J. Penn, 89
- Kuhn, J. R., Penn, M. J., & Mann, I. 1996, *ApJL*, 456, L67, doi: [10.1086/309864](https://doi.org/10.1086/309864)
- Kuhn, J. R., MacQueen, R. M., Streete, J., et al. 1999, *ApJ*, 521, 478, doi: [10.1086/307529](https://doi.org/10.1086/307529)
- Lin, H., Kuhn, J. R., & Coulter, R. 2004, *ApJL*, 613, L177, doi: [10.1086/425217](https://doi.org/10.1086/425217)
- Mikhailenko, S., Kassi, S., Mondelain, D., Gamache, R., & Campargue, A. 2016, *Journal of Quantitative Spectroscopy and Radiative Transfer*, 179, 198, doi: [10.1016/j.jqsrt.2016.03.035](https://doi.org/10.1016/j.jqsrt.2016.03.035)
- Morton, R. J., Tomczyk, S., & Pinto, R. 2015, *Nature Communications*, 6, 7813, doi: [10.1038/ncomms8813](https://doi.org/10.1038/ncomms8813)
- Münch, G. 1966, *ApJ*, 145, 237, doi: [10.1086/148758](https://doi.org/10.1086/148758)
- Nagata, S., Tsuneta, S., Suematsu, Y., et al. 2008, *ApJL*, 677, L145, doi: [10.1086/588026](https://doi.org/10.1086/588026)
- Naumenko, O. V., & Horneman, V.-M. 2019, $^{32}\text{S}^{16}\text{O}_2$ line list
- Nelson, P. G., Casini, R., de Wijn, A. G., & Knoelker, M. 2010, in SPIE Conference Series, Vol. 7735, Ground-based and Airborne Instrumentation for Astronomy III, 77358C, doi: [10.1117/12.857610](https://doi.org/10.1117/12.857610)
- Oliva, E., Marconi, A., Maiolino, R., et al. 2001, *A&A*, 369, L5, doi: [10.1051/0004-6361:20010214](https://doi.org/10.1051/0004-6361:20010214)
- Olsen, K. H., Anderson, C. R., & Stewart, J. N. 1971, *SoPh*, 21, 360, doi: [10.1007/BF00154287](https://doi.org/10.1007/BF00154287)
- Parashiv, A. R., & Judge, P. G. 2022, In rev, *SoPh Penn*, Matthew J., K. 2014, *Living Reviews in Solar Physics*, 11, 2, doi: [10.12942/lrsp-2014-2](https://doi.org/10.12942/lrsp-2014-2)
- Penn, M. J., & Kuhn, J. R. 1994, *ApJ*, 434, 807, doi: [10.1086/174784](https://doi.org/10.1086/174784)
- Penn, M. J., Kuhn, J. R., Arnaud, J., Mickey, D. L., & Labonte, B. J. 1994, *SSRv*, 70, 185, doi: [10.1007/BF00777865](https://doi.org/10.1007/BF00777865)
- Pierce, A. K. 1964, *ApOpt*, 3, 1337, doi: [10.1364/AO.3.001337](https://doi.org/10.1364/AO.3.001337)
- Plowman, J. 2014, *ApJ*, 792, 23, doi: [10.1088/0004-637X/792/1/23](https://doi.org/10.1088/0004-637X/792/1/23)
- Rempel, M. 2011, *ApJ*, 740, 15, doi: [10.1088/0004-637X/740/1/15](https://doi.org/10.1088/0004-637X/740/1/15)
- Rimmele, T. R., Warner, M., Keil, S. L., et al. 2020, *SoPh*, 295, 172, doi: [10.1007/s11207-020-01736-7](https://doi.org/10.1007/s11207-020-01736-7)
- Samra, J. E., Judge, P. G., DeLuca, E. E., & Hannigan, J. W. 2018, *ApJL*, 856, L29, doi: [10.3847/2041-8213/aab434](https://doi.org/10.3847/2041-8213/aab434)
- Samra, J. E., Marquez, V., Cheimets, P., et al. 2021, arXiv e-prints, arXiv:2105.09419. <https://arxiv.org/abs/2105.09419>
- Schiffmann, S., Brage, T., Judge, P. G., Parashiv, A. R., & Wang, K. 2021, *ApJ*, 923, 186, doi: [10.3847/1538-4357/ac2cca](https://doi.org/10.3847/1538-4357/ac2cca)
- Singh, J., Sakurai, T., Ichimoto, K., & Takeda, A. 2002, *PASJ*, 54, 807, doi: [10.1093/pasj/54.5.807](https://doi.org/10.1093/pasj/54.5.807)
- Tennyson, J., Bernath, P., Brown, L., et al. 2013, *Journal of Quantitative Spectroscopy and Radiative Transfer*, 117, 29, doi: [10.1016/j.jqsrt.2012.10.002](https://doi.org/10.1016/j.jqsrt.2012.10.002)
- Thompson, M. J., Tomczyk, S., Gibson, S. E., McIntosh, S. W., & Landi, E. 2018, in IAU Symposium, Vol. 335, Space Weather of the Heliosphere: Processes and Forecasts, ed. C. Foullon & O. E. Malandraki, 359–361, doi: [10.1017/S1743921317011334](https://doi.org/10.1017/S1743921317011334)
- Tomczyk, S., & Landi, E. 2019, in Solar Heliospheric and Interplanetary Environment (SHINE 2019), 131
- Tomczyk, S., McIntosh, S. W., Keil, S. L., et al. 2007, *Science*, 317, 1192, doi: [10.1126/science.1143304](https://doi.org/10.1126/science.1143304)

- Toth, R. 1995a, Linelist of water vapor parameters from 500 to 8000 cm^{-1} . <http://mark4sun.jpl.nasa.gov/h2o.html>
- . 1995b, Linelist of N_2O parameters from 500 to 7500 cm^{-1} . <http://mark4sun.jpl.nasa.gov/n2o.html>
- Wallace, L., Livingston, W., Hinkle, K., & Bernath, P. 1996, ApJS, 106, 165, doi: [10.1086/192333](https://doi.org/10.1086/192333)
- Welsch, B. T., Fisher, G. H., & Sun, X. 2013, ApJ, 765, 98, doi: [10.1088/0004-637X/765/2/98](https://doi.org/10.1088/0004-637X/765/2/98)
- Zhang, J., Dere, K. P., Howard, R. A., & Vourlidas, A. 2004, ApJ, 604, 420, doi: [10.1086/381725](https://doi.org/10.1086/381725)
- Zhang, Q. M., Huang, Z. H., Hou, Y. J., et al. 2021, A&A, 647, A113, doi: [10.1051/0004-6361/202038924](https://doi.org/10.1051/0004-6361/202038924)

APPENDIX

A. SPECTROSCOPY AND CDF FITTING FOR ALL LINES DISCUSSED

This section contains detailed spectroscopic plots of the spectral regions of interest and the best fits for each candidate of the Fe XIII, Si X, and Si IX absorption lines. Each spectral region is also individually convolved with a Gaussian function correspondent to the Cryo-NIRSP 0.5 slit spectral resolution, as dependent on the appropriate filter. In addition, we show the individual CDF fits of all identified photospheric and atmospheric absorptions.

A.1. Fe XIII 1074.68 nm spectral window

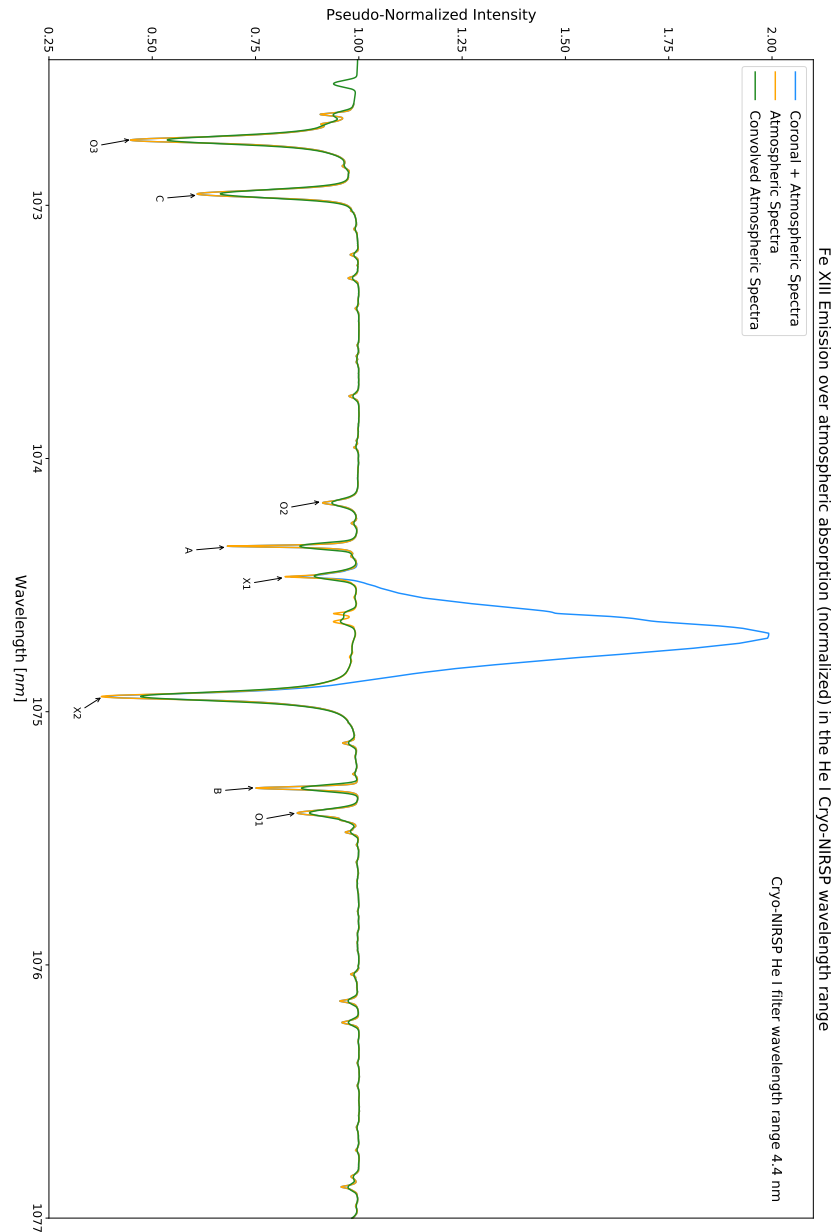


Figure 6. Fe XIII 1074.68 nm emission over atmospheric absorption (normalized) in the He I Cryo-NIRSP wavelength range with all labeled candidate lines in Table 3. The green curve represents the atmospheric spectra that is convolved with a Gaussian function correspondent to the Cryo-NIRSP 0.5 slit spectral resolution of 0.027 nm of the He I filter (see [1]).

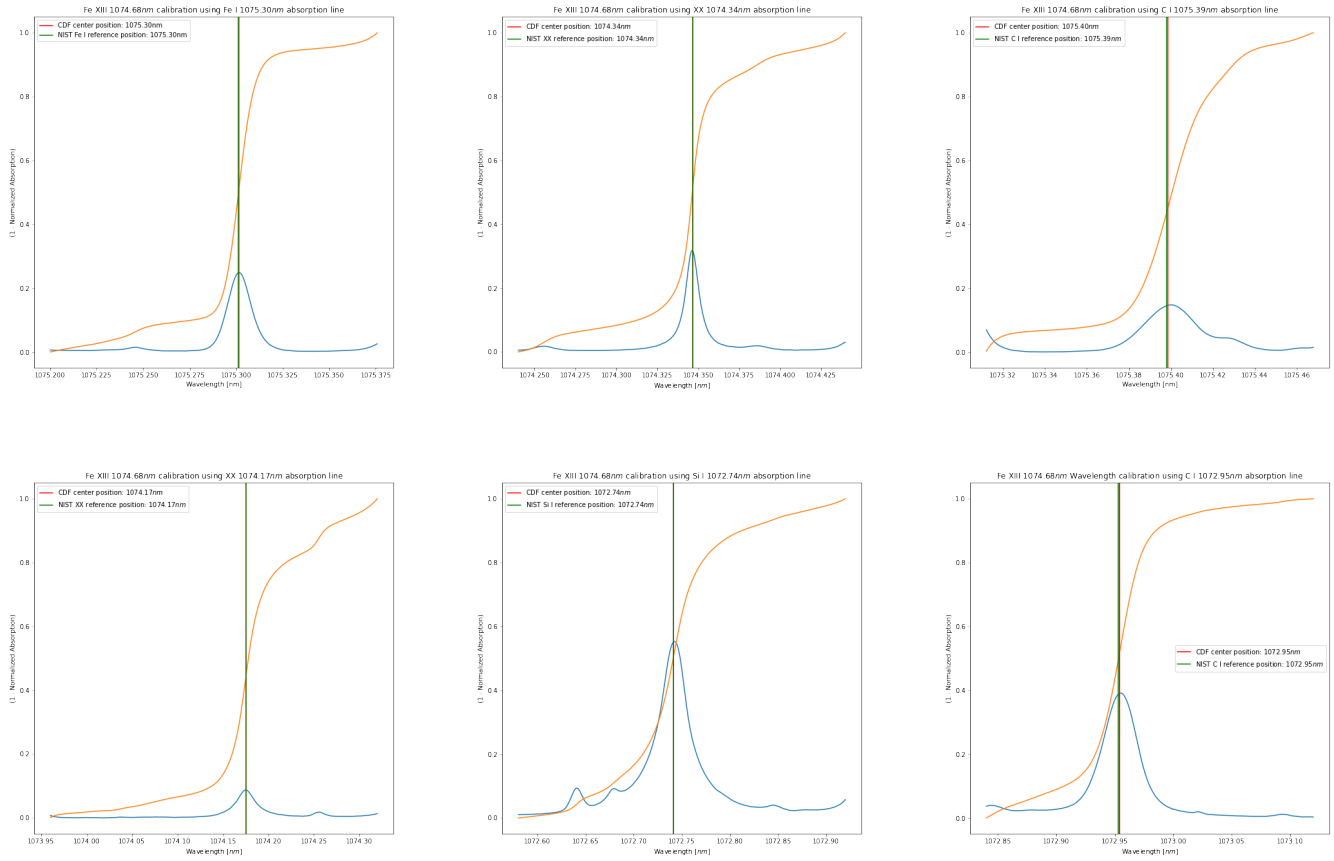


Figure 7. Fe XIII 1074.68 nm spectral window individual absorption line CDF fits. The A, B, C labeled lines as well as O1, O2, O3 are plotted. The CDF counts shown in orange are normalized to a range between 0 and 1. Note that the absorption profiles are reversed into emission to make the plot more easily readable.

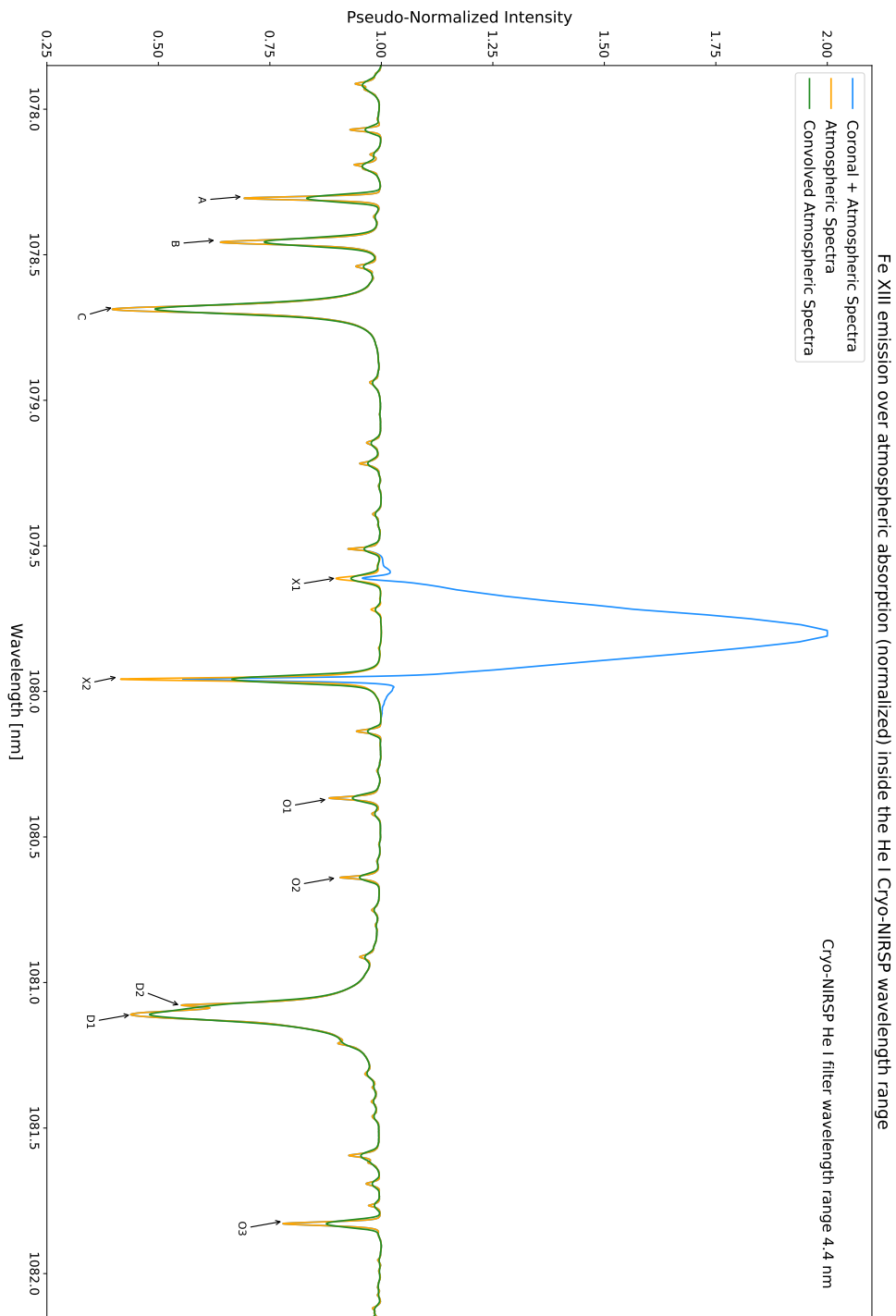
A.2. *Fe XIII 1079.79 nm spectral window*

Figure 8. Fe XIII 1079.79 nm emission over atmospheric absorption (normalized) in the He I Cryo-NIRSP wavelength range with all labeled candidate lines in Table 3. The green curve represents the atmospheric spectra that is convolved with a Gaussian function correspondent to the Cryo-NIRSP $0''.5$ slit spectral resolution of 0.027 nm of the He I filter (see [1]).

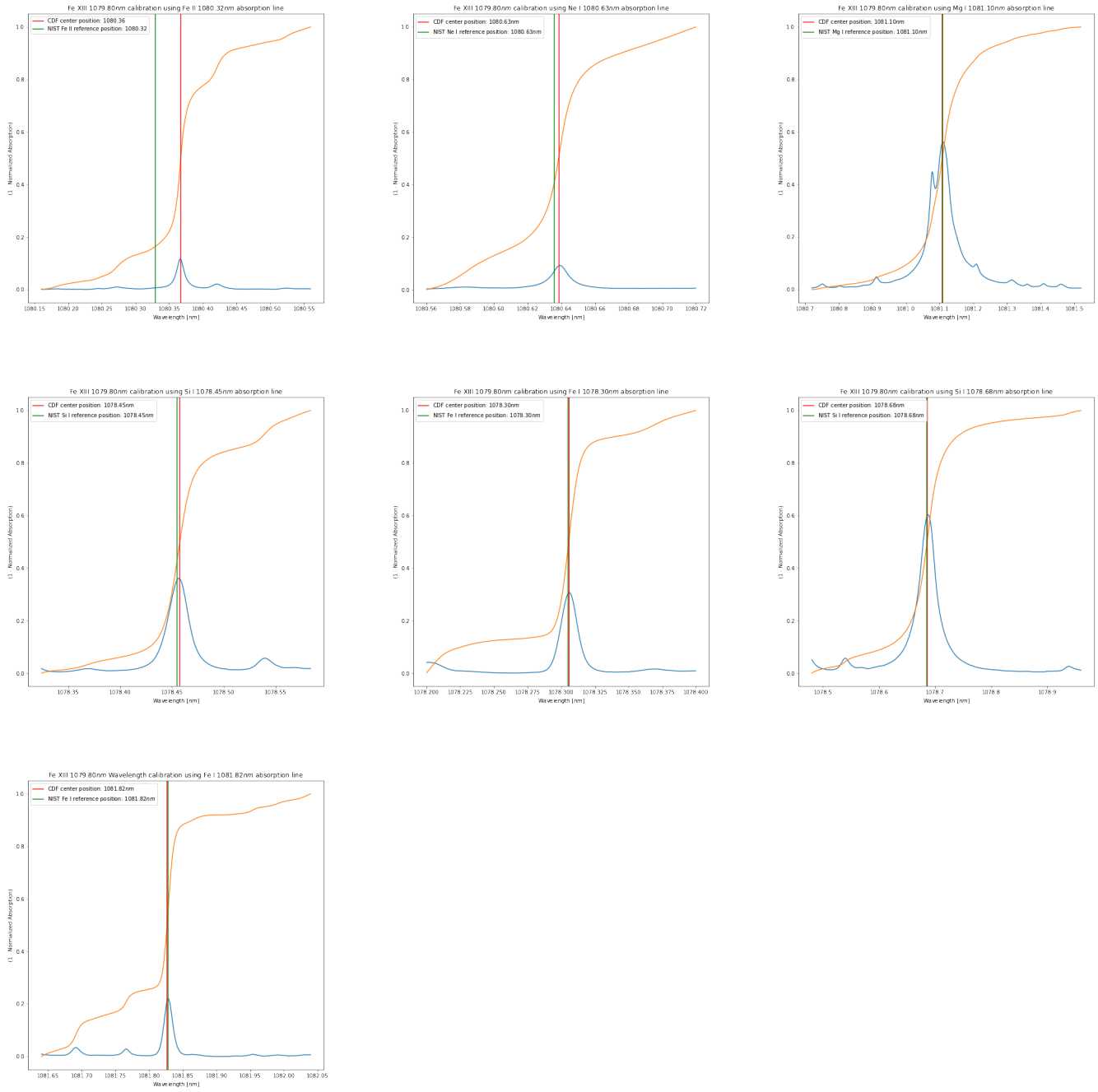


Figure 9. Fe XIII 1079.79 nm spectral window individual absorption line CDF fits. The A, B, C, D1 & 2 labeled lines as well as O1, O2, O3 are plotted. The CDF counts shown in orange are normalized to a range between 0 and 1. Note that the absorption profiles are reversed into emission to make the plot more easily readable.

A.3. Si X 1430.10 nm spectral window

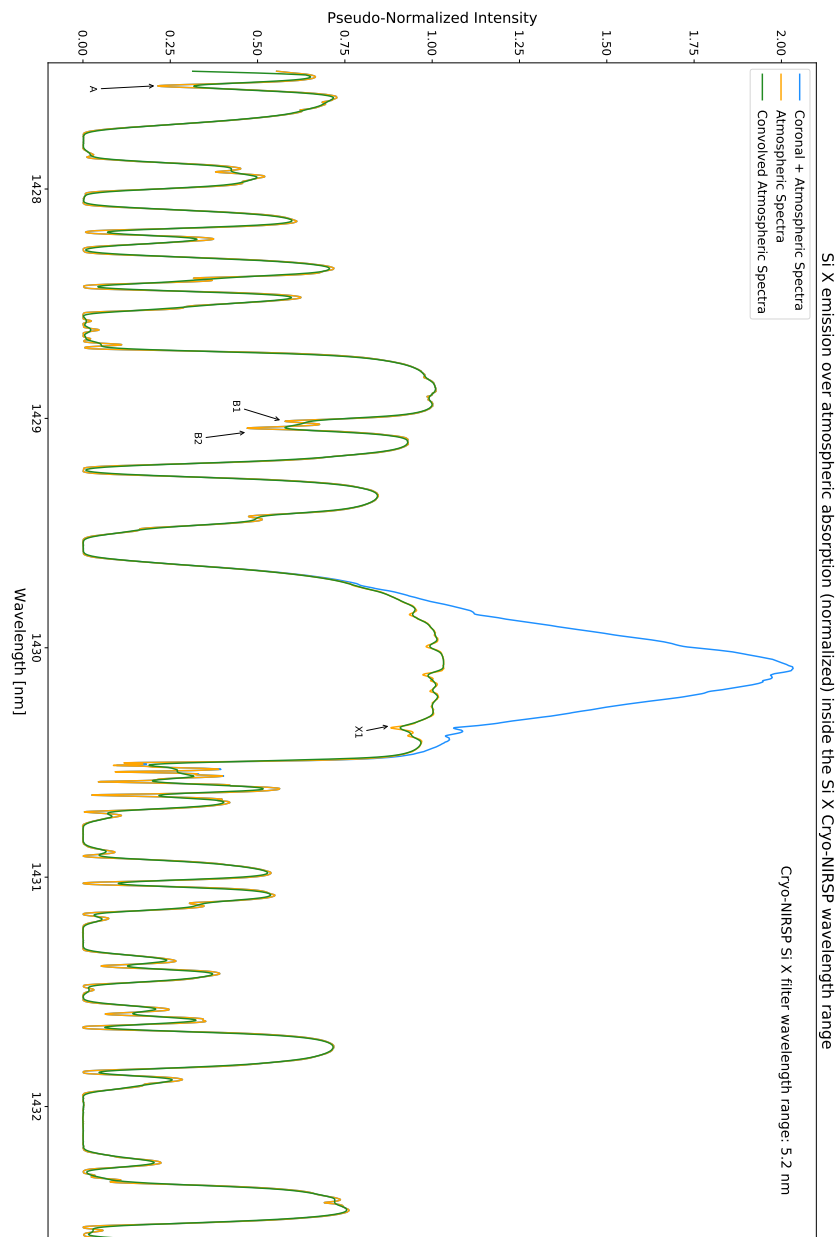


Figure 10. Si X 1430.10 nm emission over atmospheric absorption (normalized) in the Si X Cryo-NIRSP wavelength range with all labeled candidate lines in Table 3. The green curve represents the atmospheric spectra that is convolved with a Gaussian function correspondent to the Cryo-NIRSP 0.5 slit spectral resolution of 0.033 nm of the Si X filter(see [1]).

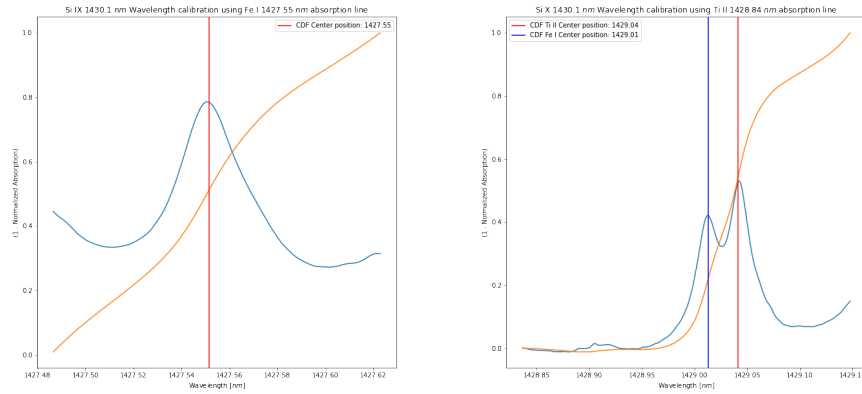


Figure 11. Si X 1430.10 nm spectral window individual absorption line CDF fits. The A, B1 & 2 labeled lines are plotted. Only few lines proved suitable due to the convoluted spectral region. The CDF counts shown in orange are normalized to a range between 0 and 1. Note that the absorption profiles are reversed into emission to make the plot more easily readable.

A.4. Si IX 3934.34 nm spectral window

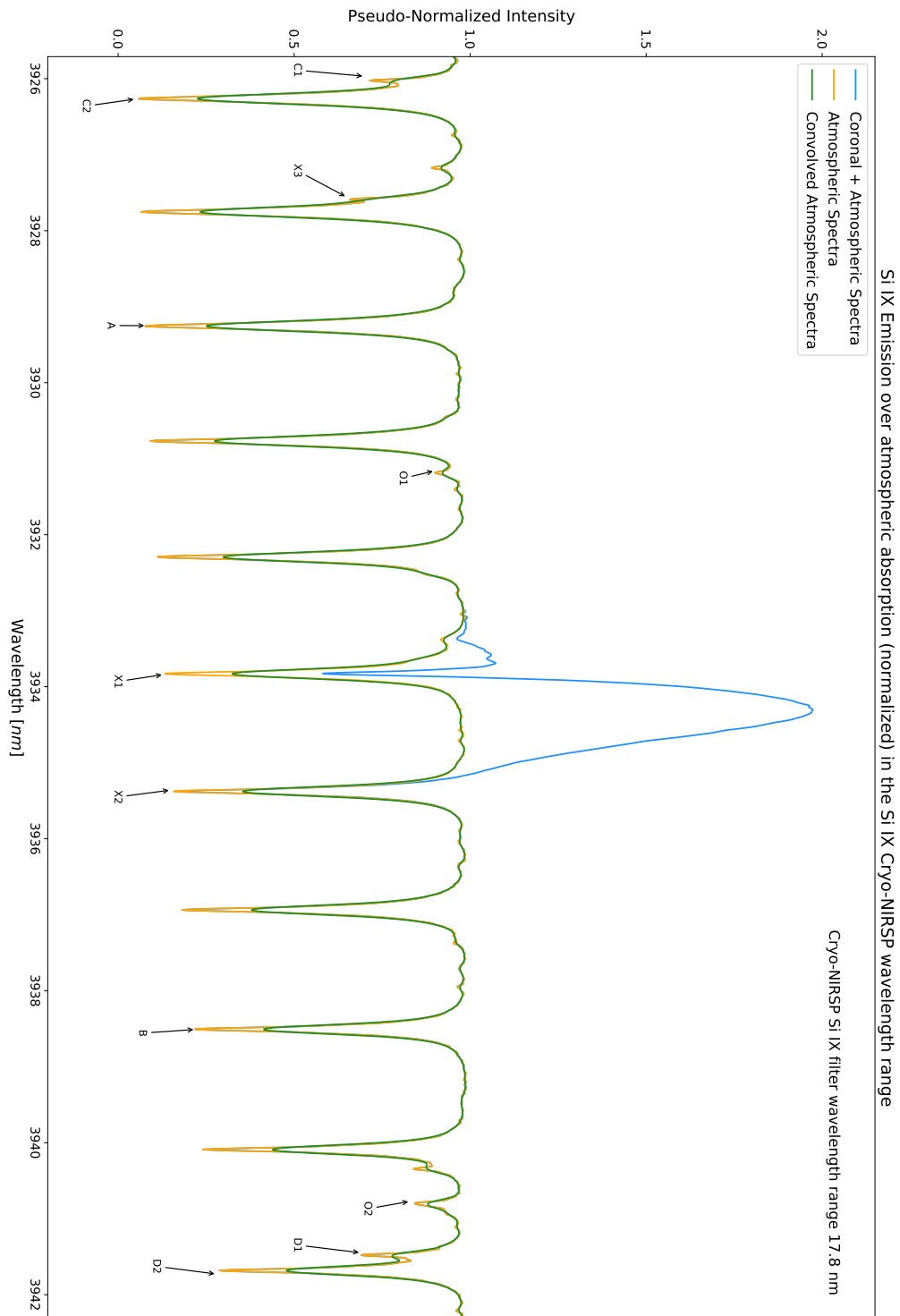


Figure 12. Si IX 3934.34 nm emission over atmospheric absorption (normalized) in the Si IX Cryo-NIRSP wavelength range with all labeled candidate lines in Table 3. The green curve represents the atmospheric spectra that is convolved with a Gaussian function correspondent to the Cryo-NIRSP 0.5 slit spectral resolution of 0.107 nm of the Si IX filter (see [1]).

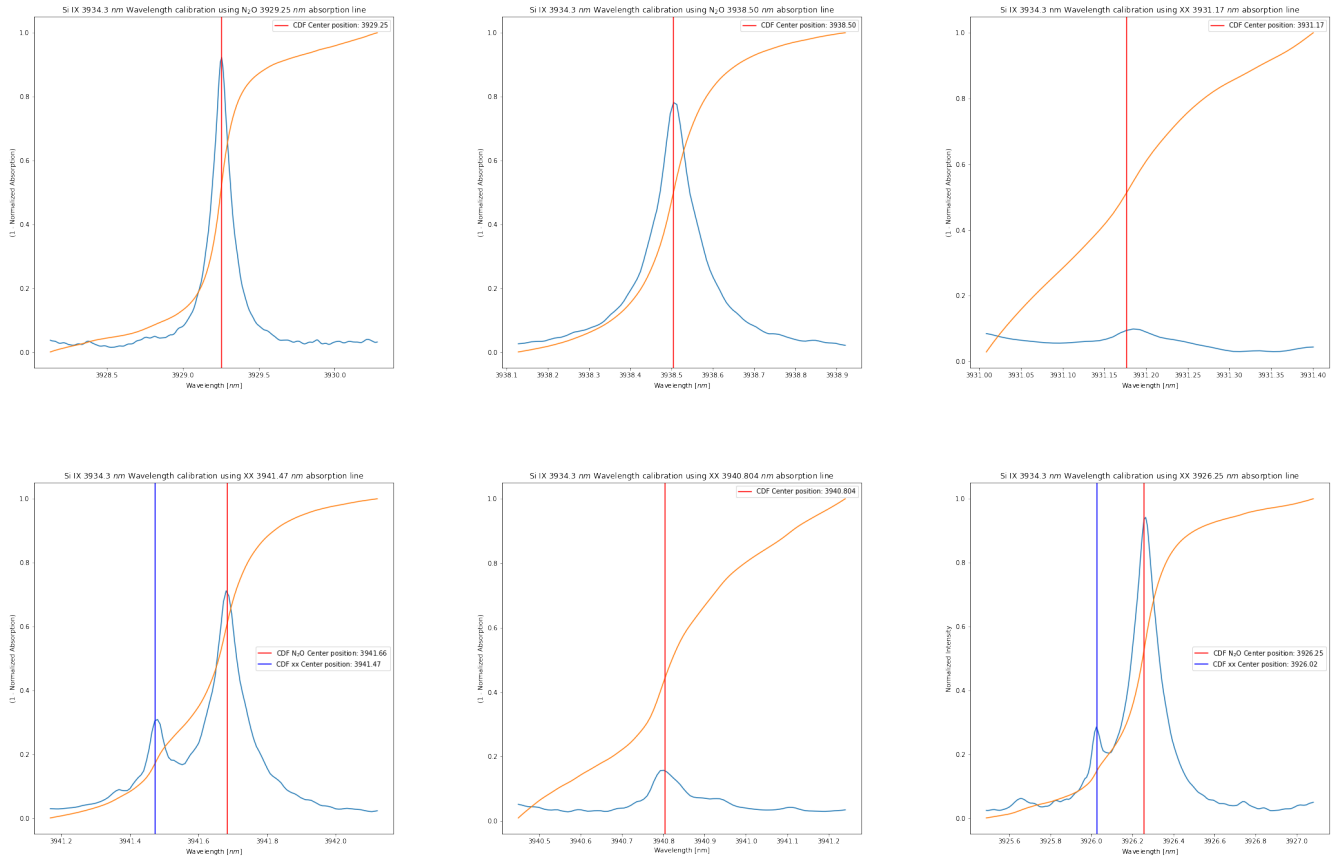


Figure 13. Si IX 3934.34 nm spectral window individual absorption line CDF fits. The A, B, C1 & 2, D1 & 2 labeled lines as well as O1, O2 are plotted. The CDF counts shown in orange are normalized to a range between 0 and 1. Note that the absorption profiles are reversed into emission to make the plot more easily readable.